



**UNIVERSIDADE FEDERAL DE CAMPINA GRANDE
PRÓ-REITORIA DE PÓS-GRADUAÇÃO
CENTRO DE TECNOLOGIA E RECURSOS NATURAIS
PROGRAMA DE PÓS-GRADUAÇÃO EM EXPLORAÇÃO
PETROLÍFERA E MINERAL**



DISSERTAÇÃO DE MESTRADO

**VARIAÇÃO ESPACIAL E ANÁLISE TOPOLÓGICA EM BANDAS DE
DEFORMAÇÃO NA BACIA RIO DO PEIXE, NORDESTE DO BRASIL:
IMPACTO DAS CONEXÕES NA PERMEABILIDADE**

Autora:

RAQUEL BEZERRA RODRIGUES DE MELO FREITAS

Orientador:

Prof. Dr. Francisco César Costa Nogueira (PPGEPM/UFCG)

Coorientador:

Prof. Dr. David Lino Vasconcelos (PPGEPM/UFCG)

Campina Grande - Paraíba

Fevereiro de 2023



**UNIVERSIDADE FEDERAL DE CAMPINA GRANDE
PRÓ-REITORIA DE PÓS-GRADUAÇÃO
CENTRO DE TECNOLOGIA E RECURSOS NATURAIS
PROGRAMA DE PÓS-GRADUAÇÃO EM EXPLORAÇÃO
PETROLÍFERA E MINERAL**



DISSERTAÇÃO DE MESTRADO

**VARIAÇÃO ESPACIAL E ANÁLISE TOPOLÓGICA EM BANDAS
DE DEFORMAÇÃO NA BACIA RIO DO PEIXE, NORDESTE DO
BRASIL: IMPACTO DAS CONEXÕES NA PERMEABILIDADE**

Autora:

RAQUEL BEZERRA RODRIGUES DE MELO FREITAS

Dissertação de Mestrado apresentada no dia 27 de fevereiro de 2023, ao programa de Pós-Graduação em Exploração Petrolífera e Mineral (PPGEPM) da Universidade Federal de Campina Grande (UFCG) para obtenção do grau de Mestre em Exploração Petrolífera e Mineral.

Campina Grande - Paraíba

Fevereiro de 2023

F866v

Freitas, Raquel Bezerra Rodrigues de Melo.

Variação espacial e análise topológica em bandas de deformação na Bacia Rio do Peixe, Nordeste do Brasil : impacto das conexões na permeabilidade / Raquel Bezerra Rodrigues de Melo Freitas. - Campina Grande, 2023.

78 f. : il. color.

Dissertação (Mestrado em Exploração Petrolífera e Mineral) - Universidade Federal de Campina Grande, Centro de Tecnologia e Recursos Naturais, 2023.

"Orientação: Prof. Dr. Francisco César Costa Nogueira, Prof. Dr. David Lino Vasconcelos."

Referências.

1. Petróleo - Reservatório. 2. Reservatórios Siliclásticos. 3. Bandas de Deformação. 4. Zona de Falha. 5. Zona de Dano. 6. Topologia. 7. Medidas de Permeabilidade. I. Nogueira, Francisco César Costa. II. Vasconcelos, Davi Lino. III. Título.

CDU 556.55(043)

Processo:
23096.008684/2023-76Documento:
3142802

MINISTÉRIO DA EDUCAÇÃO
UNIVERSIDADE FEDERAL DE CAMPINA GRANDE
POS-GRADUACAO EXP. PETROLIFERA E MINERACAO
Rua Aprigio Veloso, 882, - Bairro Universitario, Campina Grande/PB, CEP 58429-900

REGISTRO DE PRESENÇA E ASSINATURAS

ATA DA DEFESA DE DISSERTAÇÃO DE MESTRADO DE RAQUEL BEZERRA RODRIGUES DE MELO FREITAS, DO PROGRAMA DE PÓS-GRADUAÇÃO EM EXPLORAÇÃO PETROLÍFERA E MINERAL, REALIZADA EM 27 DE FEVEREIRO DE 2023.

CANDIDATA: RAQUEL BEZERRA RODRIGUES DE MELO FREITAS

COMISSÃO EXAMINADORA

ORIENTADOR E PRESIDENTE DA COMISSÃO: PROF. DR. FRANCISCO CÉZAR COSTA NOGUEIRA

EXAMINADOR EXTERNO: DR. YOE ALAIN REYES PÉREZ

EXAMINADOR EXTERNO: PROF. DR. EDSON DE ANDRADE ARAÚJO

TÍTULO DO TRABALHO: VARIAÇÃO ESPACIAL E ANÁLISE TOPOLÓGICA EM BANDAS DE DEFORMAÇÃO NA BACIA RIO DO PEIXE, NORDESTE DO BRASIL: IMPACTO DAS CONEXÕES NA PERMEABILIDADE

HORA DE INÍCIO: 14h30

LOCAL: Auditório da Unidade Acadêmica de Engenharia de Petróleo (UAEPETRO)

Em sessão pública, após exposição de cerca de 45 minutos, a candidata foi arguida oralmente pelos membros da Comissão Examinadora, tendo demonstrado suficiência de conhecimento e capacidade de sistematização, no tema de sua tese, obtendo conceito **APROVADA**. Face à aprovação, declara o presidente da Comissão, achar-se a examinada, legalmente habilitada a receber o Grau de Mestre em Exploração Petrolífera e Mineral, cabendo a Universidade Federal de Campina Grande, como de direito, providenciar a expedição do Diploma, a que a mesma faz jus. Na forma regulamentar, foi lavrada a presente ata, que é assinada por mim, ELISSANDRA NASCIMENTO DE

MOURA LIMA, e os membros da Comissão Examinadora.

Campina Grande, 27 de Fevereiro de 2023.

Recomendações: Após apresentação e sabatina da discente pela comissão de avaliação foram apresentadas sugestões para melhoria do trabalho de pesquisa. Tais sugestões foram encaminhadas para o e-mail da candidata.

ELISSANDRA NASCIMENTO DE MOURA LIMA

Coordenadora

PROF. DR. FRANCISCO CÉZAR COSTA NOGUEIRA (UFCG)

Presidente da Comissão e Orientador

PROF. DR. EDSON DE ANDRADE ARAÚJO (UFCG)

Examinador Externo

PROF. DR. YOE ALAIN REYES PÉREZ (UFRN)

Examinador Externo

RAQUEL BEZERRA RODRIGUES DE MELO FREITAS

Candidata

2 - APROVAÇÃO

2.1. Segue a presente Ata de Defesa de Dissertação de Mestrado da candidata **RAQUEL BEZERRA RODRIGUES DE MELO FREITAS**, assinada eletronicamente pela Comissão Examinadora acima identificada.



Documento assinado eletronicamente por **ELISSANDRA NASCIMENTO DE MOURA LIMA, COORDENADOR(A)**, em 01/03/2023, às 13:22, conforme horário oficial de Brasília, com fundamento no art. 8º, caput, da [Portaria SEI nº 002, de 25 de outubro de 2018](#).



Documento assinado eletronicamente por **Raquel Bezerra Rodrigues de Melo Freitas, Usuário Externo**, em 01/03/2023, às 13:29, conforme horário oficial de Brasília, com fundamento no art. 8º, caput, da [Portaria SEI nº 002, de 25 de outubro de 2018](#).



Documento assinado eletronicamente por **Yoe Alain Reyes Perez, Usuário Externo**, em 01/03/2023, às 14:19, conforme horário oficial de Brasília, com fundamento no art. 8º, caput, da [Portaria SEI nº 002, de 25 de outubro de 2018](#).



Documento assinado eletronicamente por **EDSON DE ANDRADE ARAUJO, PROFESSOR(A) DO MAGISTERIO SUPERIOR**, em 01/03/2023, às 15:33, conforme horário oficial de Brasília, com fundamento no art. 8º, caput, da [Portaria SEI nº 002, de 25 de outubro de 2018](#).



Documento assinado eletronicamente por **FRANCISCO CEZAR COSTA NOGUEIRA, PROFESSOR(A) DO MAGISTERIO SUPERIOR**, em 03/03/2023, às 10:53, conforme horário oficial de Brasília, com fundamento no art. 8º, caput, da [Portaria SEI nº 002, de 25 de outubro de 2018](#).



A autenticidade deste documento pode ser conferida no site <https://sei.ufcg.edu.br/autenticidade>, informando o código verificador **3142802** e o código CRC **E3631EA4**.

“Only those who will risk going too far can possibly find out how far one can go”.

Thomas S. Elliot

A minha amada família, minha mãe (Eleonalda), meu pai (Ronivaldo), meu irmão (Gabriel) e irmã (Sophia).

AGRADECIMENTOS

Gostaria de agradecer primeiramente a Deus, que me deu força e discernimento para continuar nos dias difíceis. Obrigada por sempre está comigo e mostrar que tudo é possível.

Meus sinceros agradecimentos aos meus pais, Eleonalda Maria Rodrigues de Aquino Freitas e Ronivaldo de Melo Freitas. Obrigada por nunca medirem os esforços para o meu melhor, por me apoiarem e me motivarem sempre. Amo vocês!

Agradeço, em especial, a minha inspiração de lutas e conquistas, minha avó Maria de Melo Freitas. Obrigada voinha pelo apoio e torcida de sempre. Amo a senhora até o infinito!

Á meus familiares e amigos que sempre estiveram na torcida pelas minhas conquistas.

Ao meu orientador, Prof. Francisco César, por todos os conhecimentos compartilhados, pela compreensão e disposição sempre que precisei. Obrigada por sempre pensar no melhor dos seus alunos, sou muita grata pelas oportunidades proporcionadas. Apesar de não ser meu orientador, David Lino Vasconcelos contribuiu e me ajudou bastante ao longo da minha caminhada, e sempre solícito.

Aos meus colegas do LAPEP, vocês tornaram meus dias mais leves e alegres. Obrigada pela troca de conhecimentos, pelo trabalho em equipe e amizade. Ah, e obrigada pelos vários copos de café ao longo do dia.

Por fim, à Petrobras/UFCG pelo financiamento do projeto de pesquisa DEBRIP: análise multiescalar e geração de banco de dados geofísico, geológico, modelagem e simulação numérica (TC 5850.0109438.18.9) ao qual minha dissertação faz parte, bem como agradeço a FAPESQPB pelo financiamento do projeto “Evolução tectônica sin e pós-rifte em bacias sedimentares intracontinentais no Nordeste do Brasil: Implicações ao estudo de análogos de reservatórios.

RESUMO

A análise topológica pode auxiliar na caracterização estrutural, bem como na compreensão da influência das conexões na propriedade de fluxo em rochas reservatório afetadas por bandas de deformação. No presente trabalho utilizamos uma exposição tridimensional (parede e piso) de uma zona de falha da falha de borda Portalegre na Bacia Rio do Peixe, Nordeste do Brasil para avaliar a influência das conexões na permeabilidade. A partir de mapeamento estrutural de detalhe, analisamos o padrão topológico das bandas de deformação. Adicionalmente, realizamos medidas de permeabilidade *in situ*. A combinação dos dados estruturais com os dados de permeabilidade nos permitiu investigar a influência da conectividade de uma rede de bandas de deformação e seu impacto nas propriedades de fluxo de fluido em uma zona de falha. Os resultados mostraram a variação do padrão de conectividade ao longo da zona de falha, com o núcleo apresentando padrão $Y > I > X$ e a zona de dano $Y > X > I$. Observamos que no núcleo, foram registrados os maiores valores de permeabilidade no nó I, seguido pelos nós Y e X. Na zona de dano, há uma variação anisotrópica, onde a parede da exposição registra maiores valores de permeabilidade para os nós I e secundariamente para os nós Y e X, enquanto no piso a permeabilidade maior foi registrada nos nós I e secundariamente nos nós X e Y. Em adição, foram identificados novos nós (com cinco e seis ramos) formados a partir do cruzamento de dois sistemas de falhas formados em diferentes fases tectônicas da bacia (sin-rifte e pós-rifte). Este estudo contribui com novas perspectivas sobre a influência das conexões de bandas de deformação na permeabilidade em uma zona de falha. Essa informação pode implicar na modelagem e simulação de reservatórios siliciclásticos afetados por zona de falha, pois possibilita avaliar o impacto da variação da conectividade no fluxo de fluido.

Palavras-chaves: Bandas de deformação, Zona de Falha, Zona de Dano, Topologia, Permeabilidade.

Abstract

Topological analysis can help in structural characterization, as well as in understanding the influence of connections on flow properties in reservoir rocks affected by deformation bands. In the present work, we used a three-dimensional exposure (wall and floor) of a fault zone in the Rio do Peixe Basin, Northeastern Brazil, to evaluate the influence of connections on permeability. From detailed structural mapping, we analyze the topological pattern of deformation bands. Additionally, we performed in situ permeability measurements. The combination of structural data with permeability data allowed us to investigate the influence of the connectivity of a deformation band network and its impact on fluid flow properties in a fault zone. The results showed the variation of the connectivity pattern along the fault zone, with the core presenting $Y>I>X$ pattern and the damage zone $Y>X>I$. We observed that in the core, the highest permeability values were recorded at I - nodes, followed by Y- and X- nodes. In the damage zone, there is an anisotropic variation, where the exposure wall registers higher permeability for I - nodes and secondarily for Y- and X- nodes, while on the floor the highest permeability was recorded at I - nodes and secondarily at X- and Y- nodes. In addition, new nodes (with five and six branches) formed from the crossing of two fault systems formed in different tectonic phases of the basin (sin-rift and post-rift) were identified. This study contributes with new perspectives about the influence of deformation band connections on permeability in a fault zone. This information may imply the modeling and simulation of siliciclastic reservoirs affected by fault zones, because possible to assess the impact of connectivity variation on fluid flow.

Keywords: Deformation Bands, Fault Zone, Damage Zone, Topology, Permeability.

SUMÁRIO

AGRADECIMENTOS	iii
RESUMO	iv
Abstract	v
SUMÁRIO	vi
LISTA DE FIGURAS E TABELAS	viii
1. Introdução	2
1.1. Apresentação	2
1.2. Estrutura da Dissertação	2
1.3. Justificativas	3
1.4. Objetivos	4
1.5. Localização da Área de Estudo	4
2. Contexto Geológico	15
2.1. Bacia Rio do Peixe	15
2.2. Bandas de Deformação na Bacia Rio do Peixe	16
3. Fundamentação Teórica	19
3.1. Zonas de Falha	19
3.2. Bandas de Deformação	21
3.3. Distribuição de bandas de deformação na zona de falha	24
3.4. Topologia	25
<i>Manuscript in preparation for submission to the Journal of Structure Geology.</i>	29
4. 3D Topological Analysis in Deformation Bands: Insights for Structural Characterization and Impact on Permeability	29
Abstract	29
4.1. Introduction	30
4.2. Geological setting	33
4.3. Methods	35
4.4. Results	38
4.4.1. Structural Mapping	38
4.4.2. Topological analysis	41
4.4.3. Permeability versus node type	51
4.5. Discussions	53

4.5.1. Implications of tectonics from the Rio do Peixe Basin in topology analysis	53
4.5.3. Implication of topological analysis for reservoirs	56
4.6. Conclusions	57
References	58
5. Conclusões e sugestões para trabalhos futuros	68
Referências	69

LISTA DE FIGURAS E TABELAS

Figura 1.1. (A) Mapa de localização da área de estudo (Bacia Rio do Peixe) na região NE do Brasil. Adaptado de Françolin et al. (1994), Nogueira et al. (2015), Nicchio et al. (2018) e Vasconcelos et al. (2021). (B) Mapa geológico da Bacia Rio do Peixe mostrando a localização do afloramento estudado (círculo vermelho); as zonas de cisalhamento: Portalegre (ZCPA) e Patos (ZCP); as três falhas principais: Malta, Portalegre e Rio Piranhas; e as sub-bacias: Brejo das Freiras (SBBF), Sousa (SBS) e Pombal (SBP) (adaptado de Vasconcelos et al., 2021).	5
Figura 2.1. Carta estratigráfica da Bacia Rio do Peixe adaptada de Silva (2014) e Rapozo et al. (2021). Legendas: AN – Antenor Navarro; S – Sousa; RP – Rio Piranhas; T – Triunfo; P – Pilões.....	16
Figura 3.1. Modelo conceitual mostrando os elementos arquiteturais de uma zona de falha e as principais estruturas que ocorrem em cada elemento arquitetural. Adaptado de Caine et al. (1996).....	20
Figura 3.2. (A) Modelo conceitual de uma zona de falha mostrando seus principais elementos arquiteturais definidos por Caine et al. (1996): núcleo da falha, zona de dano e protólito, bem como as estruturas subsidiárias. (B) Gráfico da frequência acumulada de bandas de deformação versus a distância do núcleo da falha. Adaptado de Silva et al. (2022).	21
Figura 3.3. (A) Tipos de bandas de deformação a partir da cinemática de deformação. (B) Classificação dos tipos de bandas de deformação baseados em mecanismos deformacionais: (1) Bandas de desagregação; (2) Bandas filossilicáticas; (3) Bandas cataclásticas; e (4) Bandas de dissolução e cimentação. Adaptado de Fossen et al., (2007).....	23
Tabela 1: Parâmetros de densidade de estruturas classificados de acordo com Dershowitz e Herda (1992).....	25
Figura 3.4. Diagrama ternário mostrando a proporção de tipos de nós para diferentes redes de descontinuidades: bandas de deformação (círculo azul), falhas (triângulo Laranja) e juntas (quadrado verde). Adaptado de Manzocchi (2002) e Sanderson e Nixon (2015).....	26
Figura 3.5. Modelo esquemático de uma rede de fraturas mostrando os três tipos de nós definidos por Manzocchi (2002): (1) nó X; (2) nó Y; e (3) nó I, bem como os três	

tipos de ramos, classificados por Sanderson e Nixon (2015): (1) ramos duplamente conectados (C-C); (2) ramos parcialmente conectados (I-C); e (3) ramos isolados (I-I).
27

Figure 4.1. (A) Geological map of the Rio do Peixe Basin, showing the NE-SW-striking Portalegre Shear Zone (PASZ), the E-W-striking Patos Shear Zone (PSZ). The main border faults are the E-W-striking Malta Fault (MF), NE-SW-striking Portalegre Fault (PAF), and the NE-SW-striking Rio Piranhas Fault (RPF). The sub-basins are, from west to east are the Brejo das Freiras sub-basin (BFSB), Sousa sub-basin (SBS), and Pombal sub-basin (PSB) respectively (adapted from Nogueira et al., 2015; Torabi et al., 2021; Vasconcelos et al., 2021). The map also locates the study area of this work (red circle). (B) Unmanned Aerial Vehicle image (UAV) of the outcrop integrated with the main deformation bands clusters mapped in the fault zone (black lines). The studied portion of the fault zone is highlighted in the red square. Stereonet shows the average orientation of deformation bands, as well as slickenlines and sedimentary bedding. N = number of measurements (adapted from Nogueira et al., 2021 and Souza et al., 2022).32

Figure 4.2. (A) Drone image with a view of the XZ plane (wall) and (B) XY plane, showing the location of the circular areas and the boundary of the damage zone (white line) and the fault core (green line). The fault core is highlighted in grey with green circular areas, while the damage zone has red circular areas. The yellow lines represent linear scanlines used for determining the P10 in Figure 4.5. The A-A' segment represent XZ plane scanline and B-B' segment represent XY plane scanline. The smaller circles represent the location of permeability acquisition at each connection: node X (blue), node Y (red) and node I (green).37

Figure 4.3. (A) Schematic representation of the topology in a deformation band network, showing the types of branches and nodes in the AB segment (adapted from Sanderson and Nixon, 2015; Saevik and Nixon, 2017). (B) Bxy system refers to the terms used for the branches. The line represents the dimension of the sampling region and the columns show the dimension of deformation bands.37

Figure 4.4. Characterization of the two fault systems present in the (A) XZ Plane and (B) XY Plane of the Melancias Outcrop. The red lines represent the structures formed by the Syn-rift System and the blue lines highlight the structures of the Post-rift System. The nodes of Figure 4.7 and Figure 4.8 are located by the black arrows.39

Figure 4.5. Graph of frequency and cumulative frequency of deformation bands recorded in the scanline (yellow line in Fig. 4.4) the XZ plane (Figura 4.4A) (adapted from Souza et al. 2022) and the XY plane (Figure 4.4B). d.z.1 = damage zone 1; z.d.2 = damage zone 2.....40

Figure 4.6. Schematic model for a deformation band network showing the types of nodes previously discussed (Sanderson and Nixon, 2015; Saevik and Nixon, 2017) and the new nodes found in this study (H and W nodes).41

Figure 4.7. Characterization of the intersection of five deformation band branches at the same point (H-node). (A, C) Outcrop wall images and (B, D) schematic drawing showing the H-node, where is observed the intersection of five branches of deformation bands at the same point. The location of the photographed points can be seen in Figure 4.4.42

Figure 4.8. Characterization of the intersection of six deformation band branches at the same point (W-node). (A, C, E) The portion of the outcrop without interpretation, and (B, D, F) schematic drawing showing the W-nodes. The location of A, C, and E can be seen in Figure 4.4.....43

Figure 4.9. Ternary diagram showing the proportion of nodes in the architectural elements of the fault zone (core and damage zone) to the (A) XZ plane and (B) XY plane. The symbols in red are referring to the data of the circular areas disposed of in the damage zone and the orange symbols represent the fault core data.44

Figure 4.10. Topological map with the number of connections for the (A) XZ plane (wall) and (B) XY plane (floor) of the outcrop. The purple outline limits the analyzed area and the reddish color regions represent a higher number of connections. The green dashed line represents the fault core in the XZ plane and the white dashed line represents the fault core in the XY plane.46

Figure 4.11. Topological map of the number of branches for the XZ plane (A) and XY plane (B) of the studied outcrop. The regions with darker coloration present a greater number of branches. The purple outline limits the analyzed area and the reddish color regions represent a higher number of branches. The green dashed line represents the fault core in the XZ plane and the white dashed line represents the fault core in the XY Plane.47

Figure 4.12. Detail of the topology for the XZ Plane (wall) circular scanlines, showing the percentage of different types of nodes for each area and the branches formed by the connections. The location of scanlines ares is in Figure 4.2A.48

Table 4.1. Average values of topological parameters between the XY (wall) and XZ (floor) planes for the core and damage zone. Analyzed parameters: X-Node, Y-Node, I-Node, Number of nodes (N_N), Number of branches (N_B), Connecting node frequency (N_C), Dimensionless intensity (B_{20}), Isolated branches (I-I), Partly connected branches (I-C), Doubly connected branches (C-C).	50
Table 4.2. Topological parameters of XZ plane (wall) circular scanlines. Analyzed parameters: X-Node, Y-Node, I-Node, Number of nodes (N_N), Number of branches (N_B), Connecting node frequency (N_C), Dimensionless intensity (B_{20}), Isolated branches (I-I), Partly connected branches (I-C), Doubly connected branches (C-C).	50
Table 4.3. Topological parameters of XY plane (floor) individual areas. Analyzed parameters: X-Node, Y-Node, I-Node, Number of nodes (N_N), Number of branches (N_B), Connecting node frequency (N_C), Dimensionless intensity (B_{20}), Isolated branches (I-I), Partly connected branches (I-C), Doubly connected branches (C-C).	51
Figure 4.14. Permeability graph of I-, Y-, and X-nodes present in the XZ plane (wall) and XY plane (floor). Orange rectangles show damage zone data. Blue rectangles represent core values. The black lines inside the rectangle refer to the median. The upper and lower black lines mean the maximum and minimum permeability values, respectively.	52
Figure 4.15. General schematic model of the 3D exposure of the outcrop showing (i) the predominance of Y nodes in both planes (XZ and XY); (ii) the intersection between syn-rift and post-rift fault systems; (iii) permeability variation in both planes for each type of connection.	54
4.5.2. Structural characterization of deformation bands: topological analysis	54

Capítulo 1

Introdução

1. Introdução

1.1. Apresentação

A presente dissertação de mestrado foi realizada como requisito obrigatório para obtenção do título de mestre junto ao Programa de Pós-Graduação em Exploração Petrolífera e Mineral (PPGEPM) da Universidade Federal de Campina Grande (UFCG). Esta pesquisa pretende analisar o padrão topológico tridimensional das bandas de deformação e sua influência na propriedade de fluxo de fluido em meios porosos siliciclásticos. Para tanto, foi selecionado um afloramento na Bacia Rio do Peixe (BRP), Nordeste do Brasil.

Esta pesquisa conta com o apoio do Laboratório de Pesquisa em Exploração Petrolífera (LAPEP/UFCG), cadastrado na Agência Nacional do Petróleo, Gás Natural e Biocombustíveis (ANP), sob coordenação do Prof. Dr. Francisco César Costa Nogueira. Esta dissertação teve o apoio financeiro dos projetos de Pesquisa, em parceria com a Petrobras e FAPESQPB, com títulos “Bandas de deformação Rio do Peixe (DEBRIP): análise multiescalar e geração de banco de dados geofísico, geológico, modelagem e simulação numérica”, e “Evolução tectônica sin e pós-rifte em bacias sedimentares intracontinentais no Nordeste do Brasil: Implicações ao estudo de análogos de reservatórios”, respectivamente.

1.2. Estrutura da Dissertação

Essa dissertação foi estruturada em cinco capítulos. O **Capítulo 1 (Introdução)** apresenta a Qualificação de Mestrado, descreve a justificativa e objetivos da pesquisa e localiza a área de estudo. O **Capítulo 2 (Contexto Geológico)** compreende a evolução tectônica e unidades estratigráficas da BRP, bem como um apanhado de trabalhos previamente publicados sobre bandas de deformação realizados na BRP. O **Capítulo 3 (Fundamentação Teórica)** realiza uma revisão bibliográfica acerca dos temas de zonas de falha, bandas de formação e topologia, enfatizando os conceitos e técnicas usadas na caracterização estrutural e petrofísica de bandas de deformação. O **Capítulo 4 (Resultados)** apresenta o manuscrito “*3D Topological Analysis in Deformation Bands: Insights for Structural Characterization and Impact on Permeability*” que está em fase de preparação até o momento dessa dissertação, para ser submetido na revista *Journal of Structural Geology*. Esse manuscrito

aborda a influência dos diferentes tipos de conexões em Bandas de Deformação na propriedade de fluxo de fluido. Por fim, o **Capítulo 5 (Conclusões e sugestões para trabalhos futuros)** expõe as conclusões obtidas nesse trabalho e algumas sugestões para trabalhos futuros.

1.3. Justificativas

Bandas de deformação são estruturas rúpteis formadas em rochas de alta porosidade (< 15%) (Antonellini *et al.*, 1994; Aydin, 1978; Fossen *et al.*, 2007, 2017) que ocorrem como estruturas individuais (*singles*) ou agrupadas (*cluster*), podendo ainda desenvolver superfícies de deslizamento (*slip surface*) (Fossen *et al.*, 2007; Torabi e Fossen, 2009; Balsamo *et al.*, 2010). Essas estruturas afetam diretamente as propriedades petrofísicas (permeabilidade e porosidade) das rochas hospedeiras (Parnell *et al.*, 2004; Ballas *et al.*, 2014; Romano *et al.*, 2020; Nogueira *et al.*, 2021), bem como as propriedades geomecânicas (Pontes *et al.*, 2019), podendo atuar como barreira ou conduto ao fluxo de fluidos em reservatórios (Rotevatn *et al.*, 2009; Medeiros *et al.*, 2010; Romano *et al.*, 2020; Nogueira *et al.*, 2021; Oliveira *et al.*, 2022; Souza *et al.*, 2022; Stohler *et al.*, 2022).

A análise de estruturas rúpteis é frequentemente realizada a partir de linhas e áreas de varreduras (Dershowitz e Herda, 1992). Os levantamentos de *scanlines* linear e de área fornecem informações sobre a distribuição de estruturas ao longo de zona de falhas, seja em superfície ou em poços. No entanto, esse tipo de análise ignora as conexões e ramificações formadas pelas estruturas. Nesse contexto, a análise topológica pode contribuir para a caracterização estrutural, visto que a topologia quantifica os parâmetros geométricos, bem como compreende a conectividade de estruturas planares dentro de uma rede (Sanderson e Nixon, 2015). Em adição, a influência das conexões entre as bandas de deformação nas propriedades petrofísicas de rochas reservatórios afetadas por falha ainda permanece pouco explorada. A partir do exposto, a análise topológica em zonas de falhas com bandas de deformação apresenta diversas questões que são incertas e precisam de uma abordagem mais detalhada, por exemplo: (1) Como os elementos arquiteturais de uma zona de falha (núcleo e zona de dano) controlam as conexões entre as bandas de deformação? (2) Como as conexões entre bandas de deformação variam em três dimensões (horizontalmente e verticalmente)? (3) Como as diferentes conexões entre

as bandas de deformação impacta a propriedade de fluxo de fluido (permeabilidade)? Em adição, estudos recentes com bandas de deformação têm utilizado a topologia para a caracterização estrutural (Awdal *et al.*, 2021; Gjesteland, 2020; Vagle, 2020; Wilson *et al.*, 2021; Bonato *et al.*, 2022). Porém, até o momento nenhum desses trabalhos tem abordado como as conexões entre as bandas de deformação influenciam na permeabilidade da rocha hospedeira em reservatórios siliciclásticos.

1.4. Objetivos

O presente trabalho tem como objetivos gerais analisar o padrão topológico das bandas de deformação nos elementos arquiteturais da zona de falha e investigar a influência da conectividade na permeabilidade. De forma complementar, três objetivos específicos são estabelecidos: (1) Caracterizar a geometria e conexões das bandas de deformação; (2) Análisar os parâmetros topológicos da zona de falha; (3) Identificar o impacto nos valores de permeabilidade entre as conexões das bandas de deformação mapeadas.

1.5. Localização da Área de Estudo

De acordo com o contexto apresentado nas justificativas e nos objetivos, a BRP (Figura 1.1), mostrou-se ser um cenário ideal para realizar análise topológica devido as extensas exposições rochosas ao longo de zonas de falha, inclusive com exposições em três dimensões. Adicionalmente, diversos estudos prévios realizaram caracterização estrutural e petrofísica na BRP (e.g., Araújo *et al.*, 2018; Nicchio *et al.*, 2018; Nogueira *et al.*, 2015; Pontes *et al.*, 2019; Torabi *et al.*, 2021; Silva *et al.*, 2022; Souza *et al.*, 2022). A BRP está localizada no nordeste do Brasil (Figura 1.1A), mais precisamente no extremo oeste do Estado da Paraíba. Para esse trabalho foi escolhido um afloramento (Melancias) que abrange a zona da Falha Portalegre, constituído por rochas siliciclásticas (siltitos, arenitos, arenitos conglomeráticos e conglomerados) da Formação Antenor Navarro (Figura 1.1B).

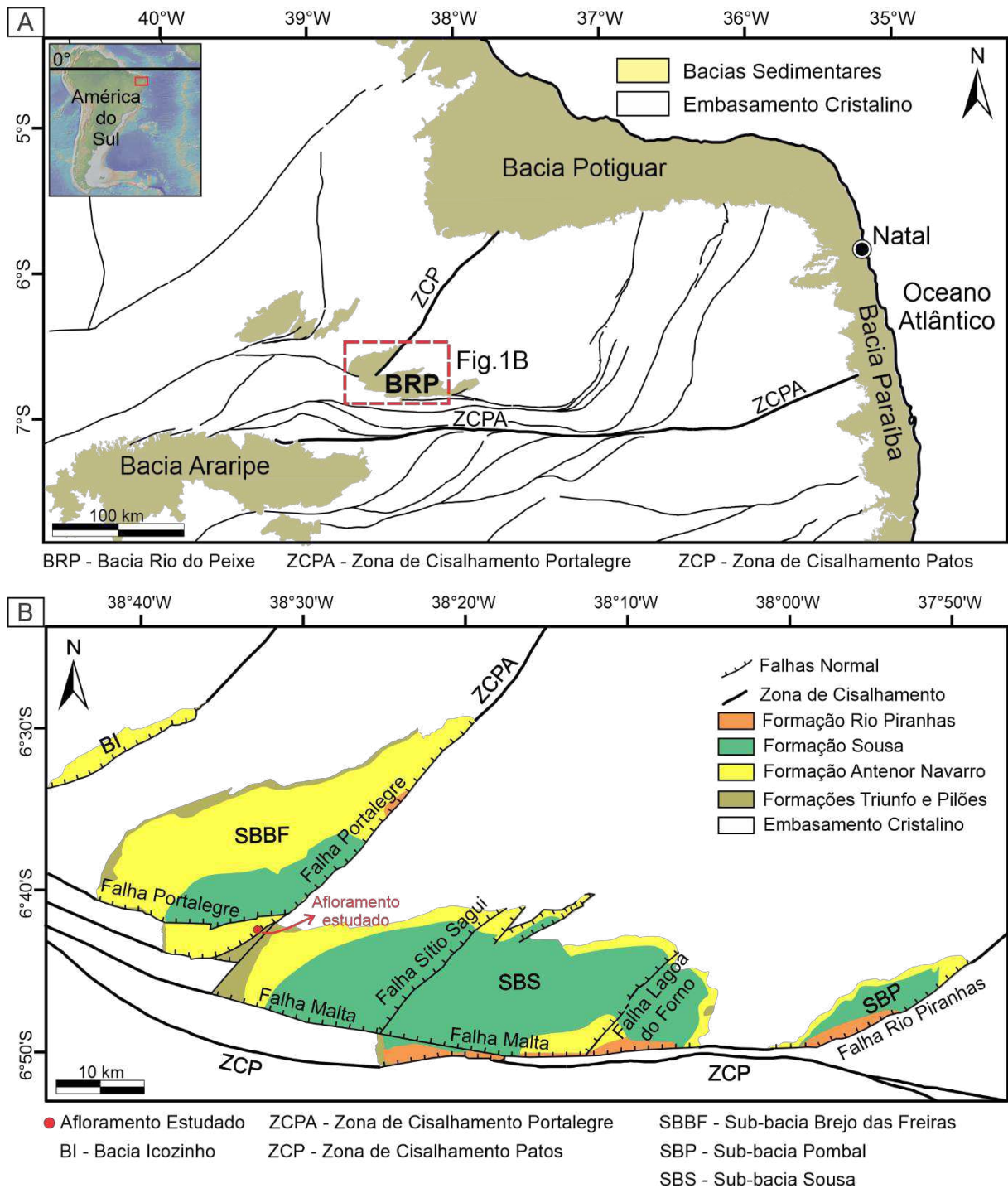


Figura 1.1. (A) Mapa de localização da área de estudo (Bacia Rio do Peixe) na região NE do Brasil. Adaptado de França *et al.* (1994), Nogueira *et al.* (2015), Nicchio *et al.* (2018) e Vasconcelos *et al.* (2021). (B) Mapa geológico da Bacia Rio do Peixe mostrando a localização do afloramento estudado (círculo vermelho); as zonas de cisalhamento: Portalegre (ZCPA) e Patos (ZCP); as três falhas principais: Malta, Portalegre e Rio Piranhas; e as sub-bacias: Brejo das Freiras (SBBF), Sousa (SBS) e Pombal (SBP) (adaptado de Vasconcelos *et al.*, 2021).

Capítulo 2

Contexto Geológico

2. Contexto Geológico

2.1. Bacia Rio do Peixe

A Bacia Rio do Peixe (BRP) (Figura 1.1), localizada no nordeste brasileiro, faz parte do conjunto de bacias interioranas de pequeno a médio porte (Françolin *et al.*, 1994). Essa bacia foi formada durante a separação do Pangeia no Cretáceo Inferior (145-130 Ma), que desencadeou um processo regional de rifteamento (Sénant e Popoff, 1991; Françolin *et al.*, 1994; de Castro *et al.*, 2007; Nogueira *et al.*, 2015; Nicchio *et al.*, 2022a). A formação da BRP ocorreu devido à reativação rúptil de zonas de cisalhamento dúcteis Neoproterozóicas de direção E-W e NE-SW, denominadas respectivamente, zonas de cisalhamento Patos e Portalegre, respectivamente (Sénant e Popoff, 1991; Françolin *et al.*, 1994; de Castro *et al.*, 2007; Nogueira *et al.*, 2015; Nicchio *et al.*, 2022a; Ramos *et al.*, 2022). Essas zonas controlaram a localização das três principais falhas de borda da BRP: as falhas Malta, Portalegre e Rio Piranhas (Nicchio *et al.*, 2022a; Ramos *et al.*, 2022). Essas falhas são responsáveis pela formação de três regiões de subsidência ou sub-bacias: Brejo das Freiras, Sousa e Pombal (Sénant e Popoff, 1991; Françolin *et al.*, 1994; de Castro *et al.*, 2007; Nogueira, *et al.*, 2015).

A evolução da BRP compreende duas fases principais: uma fase sin-rifte e uma pós-rifte (Françolin *et al.*, 1994; de Castro *et al.*, 2007; Nogueira *et al.*, 2015; Vasconcelos *et al.*, 2021; Ramos *et al.*, 2022). A fase rifte é dividida em sin-rifte I e sin-rifte II e caracterizada por processos tectônicos extensionais de direção N-S a NNE-SSE (sin-rifte I) e NW-SE (sin-rifte II) (Nicchio *et al.*, 2022a). Por outro lado, a fase pós-rifte é conhecida pela inversão tectônica da bacia, que compreende a mudança da tensão compressiva máxima (σ_1) de vertical para horizontal associada aos esforços combinados da Orogenia Andina e da Cordilheira Meso-Atlântica (Marques *et al.*, 2014; Nogueira *et al.*, 2015; Vasconcelos *et al.*, 2021).

O arcabouço estratigráfico da BRP é formado por unidades litoestratigráficas que abrangem o Grupo Rio do Peixe (Cretácio Inferior) e o Grupo Santa Helena (Devoniano Inferior), sobrepostas às rochas do embasamento cristalino Pré-cambriano (Figura 2.1) (Roesner *et al.*, 2011; Carvalho *et al.*, 2013; Silva *et al.*, 2014; Carvalho, 2020). Essas unidades são classificadas, da base para o topo: (1) Formação Pilões, composta de folhelhos e arenitos, provenientes da deposição de leques

deltaicos e flúvio deltaicos; (2) Formação Triunfo, composta por arenitos grossos a conglomeráticos cinza a esbranquiçados, com deposição flúvio-deltaico; (3) Formação Antenor Navarro, predominantemente composta de conglomerados e arenitos grossos, depositados em sistemas fluviais entrelaçados e leques aluviais; (4) Formação Sousa, constituída de folhelhos e siltitos intercalados a arenitos, depositados em ambiente lacustre, com calcários ocorrendo de forma localizada; (5) Formação Rio Piranhas, composta por conglomerados, depositados em ambientes de leques aluviais.

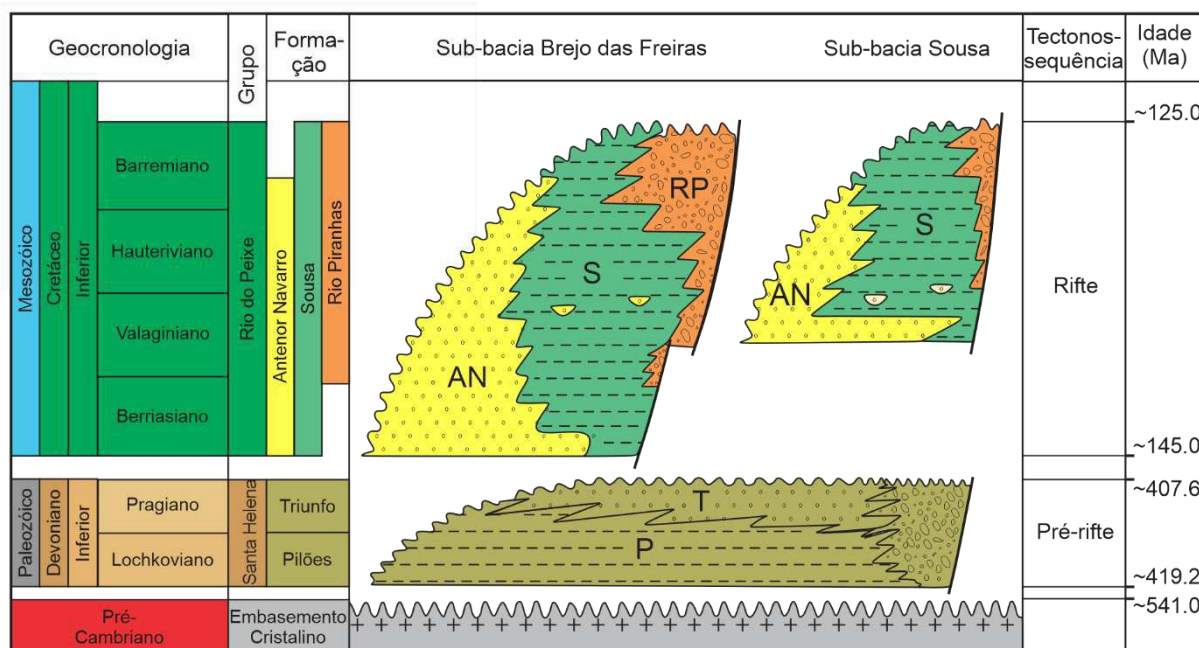


Figura 2.1. Carta estratigráfica da Bacia Rio do Peixe adaptada de Silva (2014) e Rapozo *et al.* (2021). Legendas: AN – Antenor Navarro; S – Sousa; RP – Rio Piranhas; T – Triunfo; P – Pilões.

2.2. Bandas de Deformação na Bacia Rio do Peixe

Estudos prévios sobre bandas de deformação na BRP foram realizados abordando vários assuntos: caracterização da origem das bandas de deformação (Nicchio *et al.*, 2018; de Souza *et al.*, 2021); caracterização estrutural e petrofísica de zona de falha (Araújo *et al.*, 2018; Pontes *et al.*, 2019; Nogueira *et al.*, 2021; Torabi *et al.*, 2021; Oliveira *et al.*, 2022; Silva *et al.*, 2022; Palhano *et al.*, 2023); modelagem e simulação numérica com bandas de deformação (Silva *et al.*, 2022; Stohler *et al.*, 2022; Souza *et al.*, 2022) e uso da topologia em bandas de deformação (Bonato *et al.*, 2022). Dentre os trabalhos mencionados, Nicchio *et al.* (2018) mostraram a

formação e evolução das bandas de deformação em microescala. Araújo *et al.* (2018) propuseram uma redução logarítmica na frequência da banda de deformação à medida que se distancia da zona de falha de borda do embasamento. Pontes *et al.* (2019) abordaram a variação da resistência à compressão uniaxial (UCS) e petrofísica de zonas de falhas. Nogueira *et al.* (2021) propôs que uma zona de falha pode apresentar várias texturas cataclásticas dependendo da intensidade do mecanismo de catáclase, impactando na redução da porosidade e permeabilidade. Torabi *et al.* (2021) ressaltaram que a *hard-linkage* entre os segmentos E-W e NE-SW influencia nas propriedades petrofísicas, não favorecendo o escoamento de fluidos ao longo do segmento rompido da falha. Oliveira *et al.* (2022) sugeriram como a estratigrafia mecânica influencia os elementos estruturais (frequência, geometria, espessura e mergulho em diferentes unidades mecânicas) das bandas de deformação em falhas. Silva *et al.* (2022) realizaram a modelaram 3D dos subdomínios de zona de dano de falha (zonas de dano internas e externas e zonas de transição) e fácies de falha e observaram que em direção ao protólito, ocorre redução logarítmica na frequência de bandas de deformação e aumento da permeabilidade e espaços interbandas. Souza *et al.* (2022) realizaram modelagem 2D e simulação numérica para analisar a influência das bandas de deformação no fluxo de fluidos e concluíram que essas estruturas atuam como barreiras parciais de fluxo. Stohler *et al.* (2022) mostraram através de simulações que o núcleo da falha e a zona de dano afetam negativamente o desempenho do reservatório. Palhano *et al.* (2023) analisaram os impactos das bandas de deformação e da silicificação hidrotermal nas propriedades petrofísicas de fluxo de fluido em zona de falha. Por fim, Bonato *et al.* (2022) avaliaram a influência do comprimento do traço e da orientação das bandas de deformação analisando se essas estruturas atuam como barreiras ou condutos ao fluxo de fluido em meios porosos.

Capítulo 3

Fundamentação Teórica

3. Fundamentação Teórica

3.1. Zonas de Falha

Falhas geológicas são superfícies ou descontinuidades com deslocamento cisalhante ao longo de uma zona (Tveranger *et al.*, 2004; Shipton *et al.*, 2005). Por outro lado, as falhas podem ser consideradas volumes deformados (Ma *et al.*, 2019) que possuem propriedades petrofísicas anisotrópicas ao longo de zonas de falha, podendo atuar como condutos, barreiras ou sistemas combinados de condutos e barreiras (Caine *et al.*, 1996) impactando o fluxo de fluidos em aquíferos e reservatório de petróleo (Caine *et al.*, 1996; Rotevatn *et al.*, 2007; Medeiros *et al.*, 2010). Nesse contexto, trabalhos prévios foram realizados visando compreender os elementos e distribuição dos componentes de zonas de falha (Berg e Skar, 2005; Schueller *et al.*, 2013; Choi *et al.*, 2016; Torabi *et al.*, 2019, 2020; Soliva *et al.*, 2016; Silva *et al.*, 2022).

Caine *et al.* (1996) propuseram que as zonas de falha são compostas por três elementos arquiteturais principais: (1) o núcleo da falha, (2) as zonas de dano e (3) o protólito (Figura 3.1 e 3.2A). O núcleo de uma falha é caracterizado por apresentar maior intensidade de deformação, composto por *gouge*, cataclasito, brecha, superfície de deslizamento e rochas quimicamente alteradas (Caine *et al.*, 1996; Micarelli *et al.*, 2003; Wibberley *et al.*, 2007; Braathen *et al.*, 2009; Childs *et al.*, 2009). As zonas de dano apresentam decréscimo de deformação à medida que se afasta do núcleo (Figura 3.2B), e são compostas por estruturas secundárias, como por exemplo, as bandas de deformação, juntas, e falhas de pequeno rejeito e comprimento (Berg e Skar, 2005; Faulkner *et al.*, 2010; Torabi e Berg, 2011; Choi *et al.*, 2016; Torabi *et al.*, 2019; Silva *et al.* 2022). Por outro lado, o protólito é o elemento onde as estruturas subsidiárias não ocorreram ou ocorrem em menor frequência, estando diretamente relacionado a estruturas deformacionais preexistentes (Choi *et al.*, 2016; Torabi *et al.*, 2020).

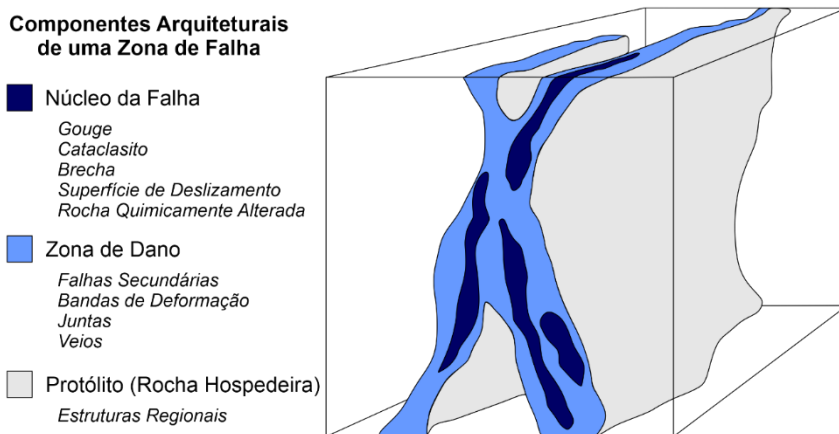


Figura 3.1. Modelo conceitual mostrando os elementos arquiteturais de uma zona de falha e as principais estruturas que ocorrem em cada elemento arquitetural. Adaptado de Caine *et al.* (1996).

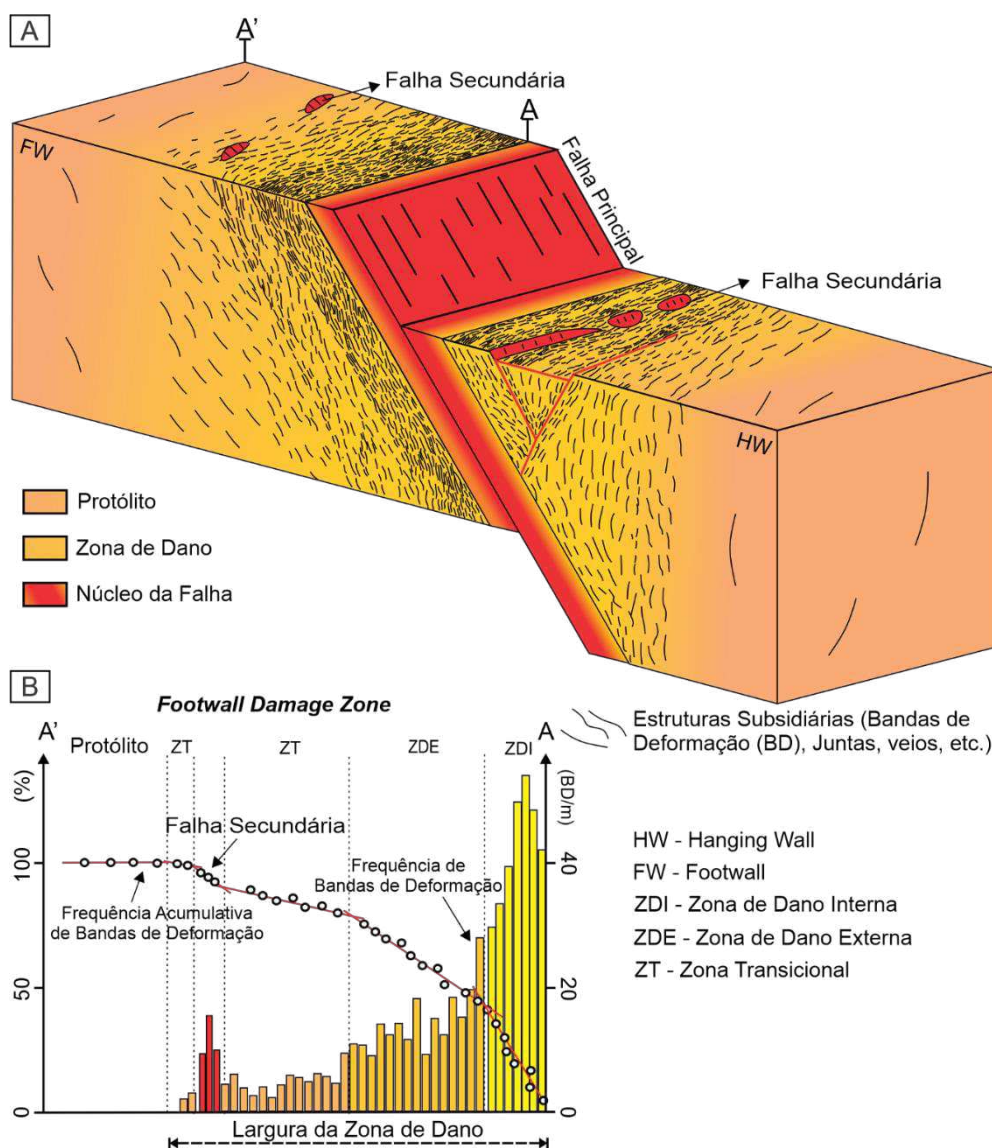


Figura 3.2. (A) Modelo conceitual de uma zona de falha mostrando seus principais elementos arquiteturais definidos por Caine *et al.* (1996): núcleo da falha, zona de dano e protólito, bem como as estruturas subsidiárias. (B) Gráfico da frequência acumulada de bandas de deformação versus a distância do núcleo da falha. Adaptado de Silva *et al.* (2022).

Em adição, Caine *et al.* (1996) sugeriram que não necessariamente todos os elementos estão presentes em uma mesma zona de falha. Nesse contexto, em arenitos porosos pouco consolidados, pequenas falhas ocorrem como bandas de deformação individuais devido a deslocamentos por cisalhamento (Aydin e Johnson, 1978; Torabi *et al.*, 2007; 2021). Conforme a deformação aumenta, duas ou mais bandas de deformação adjacentes interagem e formam uma zona mais espessa, denominada de agrupamentos de bandas de deformação (*clusters zones*) (Aydin e Johnson, 1978; Fossen *et al.*, 2007). Essa zona de bandas de deformação ocorre devido ao endurecimento por deformação (*strain hardening*), que consiste quando as bandas se tornam mais resistentes do que a rocha hospedeira (Pontes *et al.*, 2019). Por outro lado, algumas zonas de bandas de deformação são acompanhadas por uma superfície de deslizamento, que compreende uma superfície de descontinuidades composta por estrias, indicando a ocorrência de movimentações ao longo da superfície (Aydin e Johnson, 1978). As superfícies de deslizamento estão associadas ao amolecimento por deformação (*strain softening*) causado pela quebra do material que constitui as bandas de deformação (Aydin e Johnson, 1978).

3.2. Bandas de Deformação

As bandas de deformação são estruturas tabulares que ocorrem em reservatórios siliciclásticos de alta porosidade (>15%) (Aydin e Johnson, 1978; Fossen *et al.*, 2007; Torabi e Fossen, 2009) e podem atuar como barreiras ou condutos ao fluxo de fluidos em reservatórios, pois afetam as propriedades petrofísicas (Fossen *et al.*, 2007; Nogueira *et al.*, 2021), bem como as propriedades geomecânicas (Pontes *et al.*, 2019) da rocha que hospeda a deformação.

As bandas de deformação podem ser classificadas utilizando diferentes critérios. De acordo com sua cinemática de deformação (Figura 3.3A), Fossen *et al.*, (2007) classificaram as bandas de deformação em: (1) bandas de cisalhamento, (2) bandas de dilatação, (3) banda de compactação e a (4) combinação das mesmas. As

bandas de cisalhamento podem ser divididas em bandas puramente de cisalhamento, bandas de cisalhamento contracional e bandas de cisalhamento dilatacional. As bandas de dilatação e compactação compõem o grupo das estruturas que são formadas por deformação volumétrica. Bandas de compactação são suscetíveis a processos contracionais, desenvolvendo uma redução volumétrica da rocha. Em contrapartida, as bandas de dilatação estão associadas ao aumento do volume da rocha.

Adicionalmente, Fossen *et al.* (2007) classificaram as bandas de deformação utilizando os mecanismos deformacionais. Esses mecanismos dependem da mineralogia da rocha hospedeira, tamanho dos grãos, formato dos grãos, selecionamento, porosidade, cimentação e estado de tensões da rocha. De acordo com Fossen *et al.* (2007), os mecanismos de deformação dominantes são divididos em: fluxo granular (deslizamento e rotação de grãos), fluxo cataclástico (fraturamento e moagem do grão), esmerilhamento filossilicática, dissolução e cimentação, que são correlacionados, respectivamente, com bandas de desagregação, bandas cataclásticas, bandas filossilicáticas e bandas de dissolução e cimentação (Figura 3.3B).

As bandas de desagregação (Figura 3.3B1) são desenvolvidas por processos relacionados ao mecanismo de fluxo granular, que geram a rotação, deslizamentos e reorganização dos grãos. Essas bandas são difíceis de serem observadas em arenitos maciços, geralmente são encontradas em arenitos pouco consolidados. As bandas filossilicáticas ocorrem quando a quantidade de minerais filossilicáticos (argilas, micas, etc.) é maior do que 10 - 15% (Torabi, 2007). As bandas cataclásticas (Figura 3.3B2) são associadas ao rearranjo, reorientação, fraturamento, quebra e esmagamento dos grãos (Torabi e Fossen, 2009; Ballas *et al.*, 2015). Ballas *et al.* (2015) associa esses comportamentos à intensidade da catáclase, que resulta na redução de permeabilidade em diferentes ordens de magnitude. Essas estruturas apresentam núcleo deformado e mal selecionado, envolvimento de rocha compacta (Fossen *et al.*, 2007). Por outro lado, as bandas de dissolução e cimentação são formadas a partir dos processos de dissolução e cimentação (Torabi e Fossen, 2009), podendo ocorrer durante ou após a deformação (Fossen *et al.*, 2007).

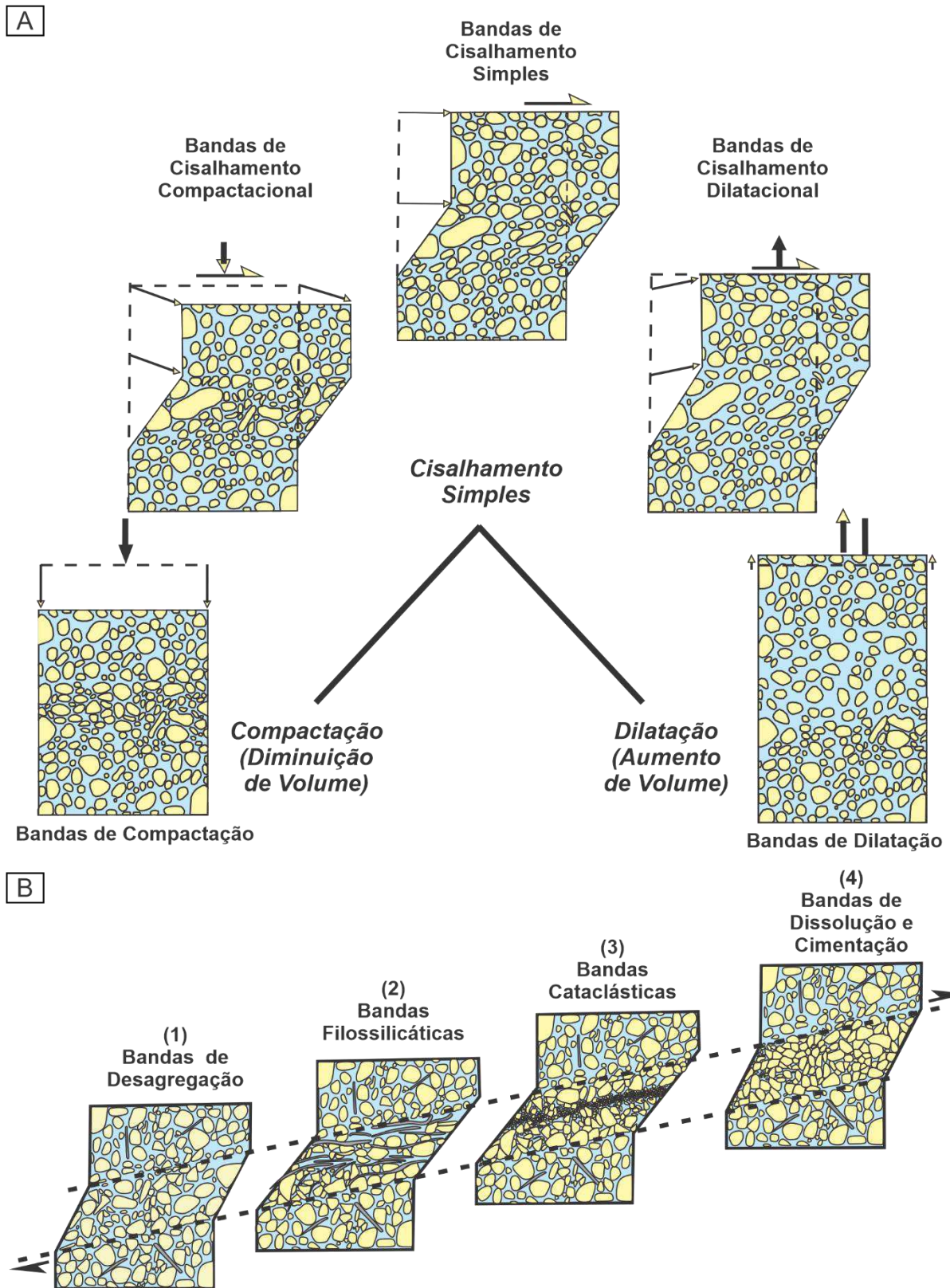


Figura 3.3. (A) Tipos de bandas de deformação a partir da cinemática de deformação. (B) Classificação dos tipos de bandas de deformação baseados em mecanismos deformacionais: (1) Bandas de desagregação; (2) Bandas filossilicáticas; (3) Bandas

cataclásticas; e (4) Bandas de dissolução e cimentação. Adaptado de Fossen *et al.*, (2007).

3.3. Distribuição de bandas de deformação na zona de falha

No que se refere a características geométricas e distribuição espacial das bandas de deformação, alguns parâmetros precisam ser descritos, tais como: orientação, mergulho, comprimento, espessura e frequência (Dershowitz e Einstein, 1988). Dentre esses parâmetros, a intensidade é de fundamental importância, pois permite comparar valores de intensidade adquiridos em diferentes regiões, utilizando os mesmos critérios de amostragem (Stohler, 2021). A intensidade de estruturas deformadas pode ser definida em diferentes dimensões, a partir da metodologia proposta por Dershowitz e Herda (1992) que consiste em um sistema P_{xy} , onde x é a dimensão de medição das estruturas e y a dimensão de amostragem (Tabela 1). A dimensão medição das estruturas pode ser realizada em contagem simples (linear), bidimensional (areal) e tridimensional (volumétrica). Por outro lado, a medição de amostragem pode ser unidimensional (linear), bidimensional (areal) e tridimensional (volumétrica) (Dershowitz e Herda, 1992).

Diversos trabalhos têm realizado a contagem da frequência de bandas de deformação em zonas de dano de falha ao longo de linhas de varredura (*scanlines*), medindo o parâmetro equivalente ao P_{10} (e.g., Araújo *et al.*, 2018; Pontes *et al.*, 2019; Torabi *et al.*, 2021; Oliveira *et al.*, 2022; Silva *et al.*, 2022; Souza *et al.*, 2022). Esses estudos mostram que ocorre o decaimento da frequência das bandas de deformação à medida que afasta do núcleo da falha. Esse decaimento é representado por modelos logarítmicos (Figura 3.2B), definidos pela equação $Y = A + L \cdot \ln(X)$, no qual “Y” consiste na frequência de estruturas e “X” a distância do núcleo da falha. No entanto, as vezes pode haver aumentos pontuais na frequência das bandas de deformação, denominado de *clusters* de bandas de deformação (Schueller *et al.*, 2013; Choi *et al.*, 2016; Soliva *et al.*, 2016).

Tabela 1: Parâmetros de densidade de estruturas classificados de acordo com Dershowitz e Herda (1992).

		Dimensão da região de amostragem		
		1: Linha	2: Área da amostra	3: Volume
Dimensão da Fratura	0: Número de estruturas	P_{10} Frequência 1D = intensidade	P_{20} Frequência 2D	P_{30} Frequência 3D
	1: Comprimento	P_{11} Intensidade Adimensional	P_{21} Intensidade de estruturas	
	2: Área da amostra		P_{22} Intensidade Adimensional	P_{32} Intensidade de estruturas
	3: Volume			P_{33} Intensidade Adimensional

Fonte: Adaptado de Dershowitz e Herda (1992).

3.4. Topologia

A topologia tem sido usada para descrever redes complexas em engenharia e redes de comunicação (Boccaletti *et al.*, 2006). No entanto, nas últimas duas décadas, a topologia tem sido aplicada em estudos para caracterizar falhas e fraturas (Manzocchi, 2002; Sanderson e Nixon, 2015; Morley e Nixon, 2016; Sanderson e Nixon, 2018; Nixon *et al.*, 2020; Silva *et al.*, 2021) e bandas de deformação (Awdal *et al.*, 2020; Gjestland, 2020; Vagle, 2020; Wilson *et al.*, 202; Bonato *et al.*, 2022). Na área da geociência, a topologia descreve as relações geométricas formadas pela interação de estruturas usando componentes, tais como os nós e ramos, e também, parâmetros adimensionais que são invariantes à escala, tensão e transformação contínua dentro da rede (Sanderson e Nixon, 2015).

No que se refere a caracterização de rede de descontinuidades, diversos trabalhos abordaram métodos para caracterizar uma rede a partir da análise topológica (e.g., Manzocchi, 2002; Sanderson e Nixon, 2015; Nyberg *et al.*, 2018).

Inicialmente, Manzocchi (2002) em seu estudo sobre a influência das características dos sistemas de fraturas secundárias na percolação de redes 2D, classificou os três tipos de nós formados pelas fraturas: (1) o nó gerado pela combinação de interseções de fraturas (nó X); (2) pilares ou aberturas (nó Y) e as pontas isoladas (nó I). Ademais, Manzocchi (2002) propôs a utilização do diagrama ternário para caracterizar a conectividade de uma rede de descontinuidades (fraturas, juntas, falhas, bandas de deformação), que consiste em um sistema com a frequência dos três tipos de nós plotados em um ponto (Figura 3.4).

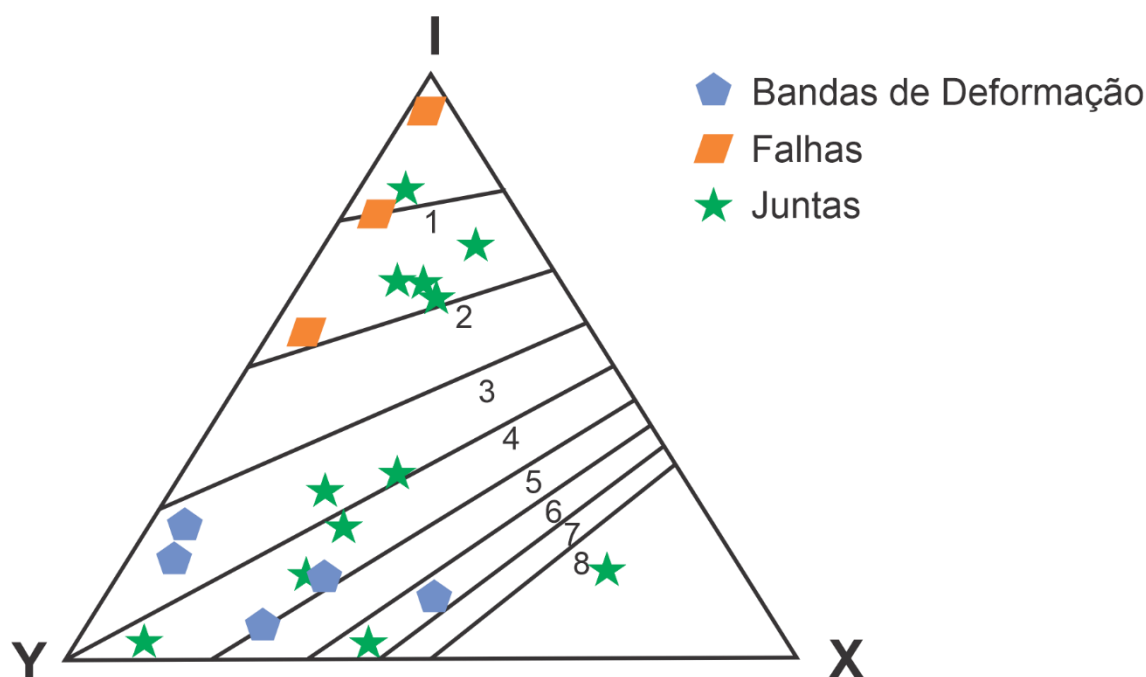


Figura 3.4. Diagrama ternário mostrando a proporção de tipos de nós para diferentes redes de descontinuidades: bandas de deformação (círculo azul), falhas (triângulo Laranja) e juntas (quadrado verde). Adaptado de Manzocchi (2002) e Sanderson e Nixon (2015).

Posteriormente, Sanderson e Nixon (2015) apresentaram algumas técnicas baseadas na contagem de nós para caracterizar uma rede de descontinuidades composta de nós e ramos (Figura 3.5). Os tipos de nós considerados nesse trabalho foram abordados anteriormente por Manzocchi (2002). Por outro lado, os ramos foram classificados em três tipos: (1) ramos parcialmente conectados, formado por um nó de conexão e um isolado (I-C); (2) ramos duplamente conectados, formado por dois nós de conexão (C-C); e ramos isolados, formado por dois nós isolados (I-I) (Sanderson e Nixon, 2015). A partir desses componentes descritos, alguns

parâmetros foram definidos para avaliar a conectividade de uma rede, tais como: número de linhas (N_L), número de ramos (N_B), relação entre o número de linhas e número de ramos (N_L/N_B), conexão por linha (C_L), número médio de ramos (C_B) (Sanderson e Nixon, 2015). Adicionalmente, foi proposto o uso da metodologia de Deshorwitz e Herda (1992) para a medição de abundância das discontinuidades, considerando a dimensão de área para a análise topológica. Porém, Sanderson e Nixon (2015) consideraram uma rede composta de linhas, nós e ramos, então, os parâmetros P_{20} , P_{21} , P_{22} foram substituídos por seus valores de ramos equivalentes, sendo respectivamente, B_{20} , B_{21} e B_{22} .

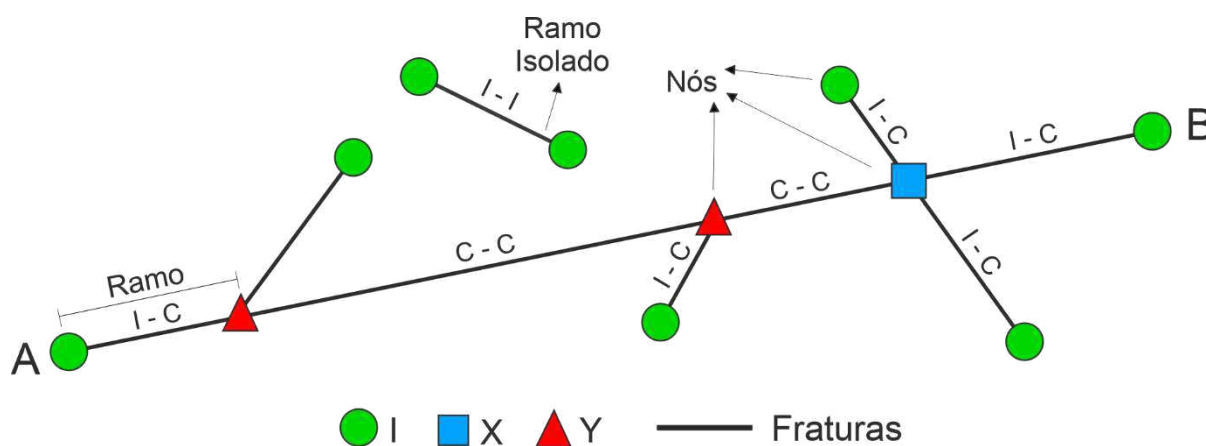


Figura 3.5. Modelo esquemático de uma rede de fraturas mostrando os três tipos de nós definidos por Manzocchi (2002): (1) nó X; (2) nó Y; e (3) nó I, bem como os três tipos de ramos, classificados por Sanderson e Nixon (2015): (1) ramos duplamente conectados (C-C); (2) ramos parcialmente conectados (I-C); e (3) ramos isolados (I-I).

Em seguida, Nyberg *et al.* (2018) projetaram a ferramenta NetworkGT que faz parte do Software QGIS, com a finalidade de incorporar a análise topológica e mitigar tempo de trabalho. Essa ferramenta permite a extração de medidas de abundância e parâmetros topológicos adimensionais usados para descrever a conectividade de uma rede, que foram abordados por Sanderson e Nixon (2015). Diante do exposto, Bonato *et al.* (2022) utilizaram essa ferramenta em seu estudo com o objetivo de analisar quantitativamente a conectividade de uma rede de bandas de deformação na Bacia Rio do peixe integrando a orientação e comprimento dessas estruturas, e por fim, avaliar as zonas mais ou menos favoráveis à migração de fluidos da área de estudo.

**Manuscript in preparation for submission to the Journal of
Structure Geology.**

Capítulo 4

***3D Topological Analysis in Deformation Bands: Insights for
Structural Characterization and Impact on Permeability***

Manuscript in preparation for submission to the Journal of Structure Geology.

4. 3D Topological Analysis in Deformation Bands: Insights for Structural Characterization and Impact on Permeability

Abstract

The structural characterization of a fault zone often focuses on determining the damage zone width. However, the deformation band connections and their impact on fluid flow properties in reservoir rocks remain poorly explored. This study used a 3D exposure of a fault zone in the Rio do Peixe Basin (NE Brazil) to investigate the impact of deformation band connection on permeability in porous sandstones. We analyzed the topological pattern of deformation bands and collected in situ permeability measurements. The results showed that the fault core concentrates more Y- and I-nodes, while the damage zone records more Y- and X-nodes. We associated the domain of Y- and I-nodes with the high intensity of deformation, which tends to organize the deformation bands, avoiding the crossing between them. In contrast, the deformation bands frequently cross in the damage zone, forming the X-nodes. Furthermore, new connections (five and six branches) formed from the intersection of two fault systems (syn-rift and post-rift). Our results record that, the I-nodes exhibit the higher permeability values and the X-nodes report the lowest. in the fault core. In the damage zone, the permeability varies according to horizontal or vertical permeability. The XZ plane (horizontal permeability) shows maximum values for I-nodes and minimum for X-nodes. The XY plane (vertical permeability) exhibits higher permeabilities for I-nodes and the lowest for Y-nodes. Therefore, this study contributes new perspectives on deformation band connections' influence on fault zones' permeability. These information can imply the modeling and simulation of siliciclastic reservoirs affected by fault zones.

Keywords: Deformation bands, Topology, Permeability, Fluid flow.

4.1. Introduction

Deformation bands are sub-seismic brittle structures formed in porous rocks (> 15% porosity) (Aydin and Johnson, 1978; Antonellini et al., 1994; Fossen et al., 2007; 2017). The deformation bands present tabular geometries that accommodate millimeter displacement, occurring as isolated structures (singles) or grouped (clusters), and may evolve into slip-surfaces associated with the faulting process (Aydin and Johnson, 1978; Torabi and Fossen, 2009; Balsamo et al., 2010; Fossen et al., 2017; de Souza et al., 2021). In the study of deformation bands, fault zones are important to understand the petrophysical properties of reservoirs. In these zones, changes the mechanical resistance (Pontes et al., 2019; Nicchio et al., 2022b; Oliveira et al., 2022; Palhano et al., 2023) influence the fluid flow properties (porosity and permeability) (Parnell et al., 2004; Ballas et al., 2014; Romano et al., 2020; Torabi et al., 2021; Silva et al., 2022), which can act as sealing structures or conduits in reservoir rocks (Rotevatn et al., 2009; Nogueira et al., 2021; Souza et al., 2022).

Fault zones present high deformation intensity and are composed of various internal structures (e.g., small faults, joints, deformation bands, breccias, gouge) (Berg and Skar, 2005; Choi et al., 2016; Rotevatn et al., 2009; Torabi et al., 2021). These zones present two main architectural elements: a fault core and a damage zone (Caine et al., 1996; Micarelli et al., 2003; Wibberley et al., 2007; Braathen et al., 2009; Childs et al., 2009). Frequently, the characterization of brittle structures composing the architectural elements of a fault zone is performed from scanlines and scan areas (Dershowitz and Herda, 1992). However, this methodology does not analyze structures connections and segments limited by nodes, defined as branches. In this context, topological analysis can contribute to the structural characterization and, consequently, understanding the influence of structure connections in the petrophysical properties of reservoirs affected by faults (Berkowitz, 1995; Jing and Stephansson, 1997). The topological analysis demonstrates the interaction of structures and quantifies geometrical parameters. Therefore, it is also applicable to deformation bands.

In deformation bands, this analysis has recently been successfully applied for structural characterization (e.g., Awdal et al., 2021; Gjesteland, 2020; Vagle, 2020; Hansberry et al., 2021; Wilson et al., 2021; Bonato et al., 2022). Several studies have been performed on deformation bands fault zones with the purpose of structural

characterization and understanding of its impacts on flow properties (porosity and permeability) (e.g., Araujo et al., 2018; Nogueira et al., 2021; Torabi et al., 2021; Oliveira et al., 2022). These studies enable the development of structural and petrophysical models and are used as input data in numerical fluid flow simulations. In this context, although deformation bands are sub-seismic structures, some studies have suggested ways to incorporate the impact of these structures on the petrophysical characteristics of geological models (e.g., Rotevatn et al., 2007; Zuluaga et al., 2016; Romano et al., 2020; Silva et al., 2022). However, studies focused on the influence of the deformation bands connections in fluid flow properties are still lacking.

The use of topological analysis in deformation bands fault zones can help to solve several questions related to the influence of architectural elements of a fault zone in reservoir properties, including: (1) How do the architectural elements of a fault zone (core and damage zone) control connections between deformation bands? (2) How do the connections vary three-dimensionally in a fault zone (fault core and damage zone)? (3) Are there other topological connections besides those described by Sanderson and Nixon (2015) and Sævik and Nixon (2017)? If so, how are these structures formed? (4) How do different connections between deformation bands impact permeability and their anisotropy?

Thus, the present study aims to analyze the topological pattern of deformation bands and investigate the influence of the connectivity of a deformation bands network on the fluid flow properties three-dimensionally, the XY (vertical permeability) and XZ (horizontal permeability) planes, respectively. We approach the structural characterization from the topological analysis and relate the different connections with the permeability along a fault zone. An outcrop in the Rio do Peixe Basin (NE Brazil) was selected as a case study (Figure 4.1). Our results enabled the identification of connections varying in the architectural elements of the fault zone. Three-dimensionally, the fault zone is dominated by Y-nodes, followed by I- and X-nodes. In addition, the fluid flow property varies according to the type of connection, with higher values for the I-node, secondarily the Y-node, and smaller values for the X-node for the core in both planes and the damage zone in the plane XZ. The damage zone in the XY plane showed higher permeabilities for I-node, followed by the X- and Y-node. Also, we reported new connections (nodes constituted five and six branches) that developed from the interaction between a syn-rift fault system and a post-rift fault

system. These results have implications for siliciclastic reservoir modeling since topology is important for understanding the connectivity of structures and, consequently, the fluid flow in porous media affected by deformation bands fault zones.

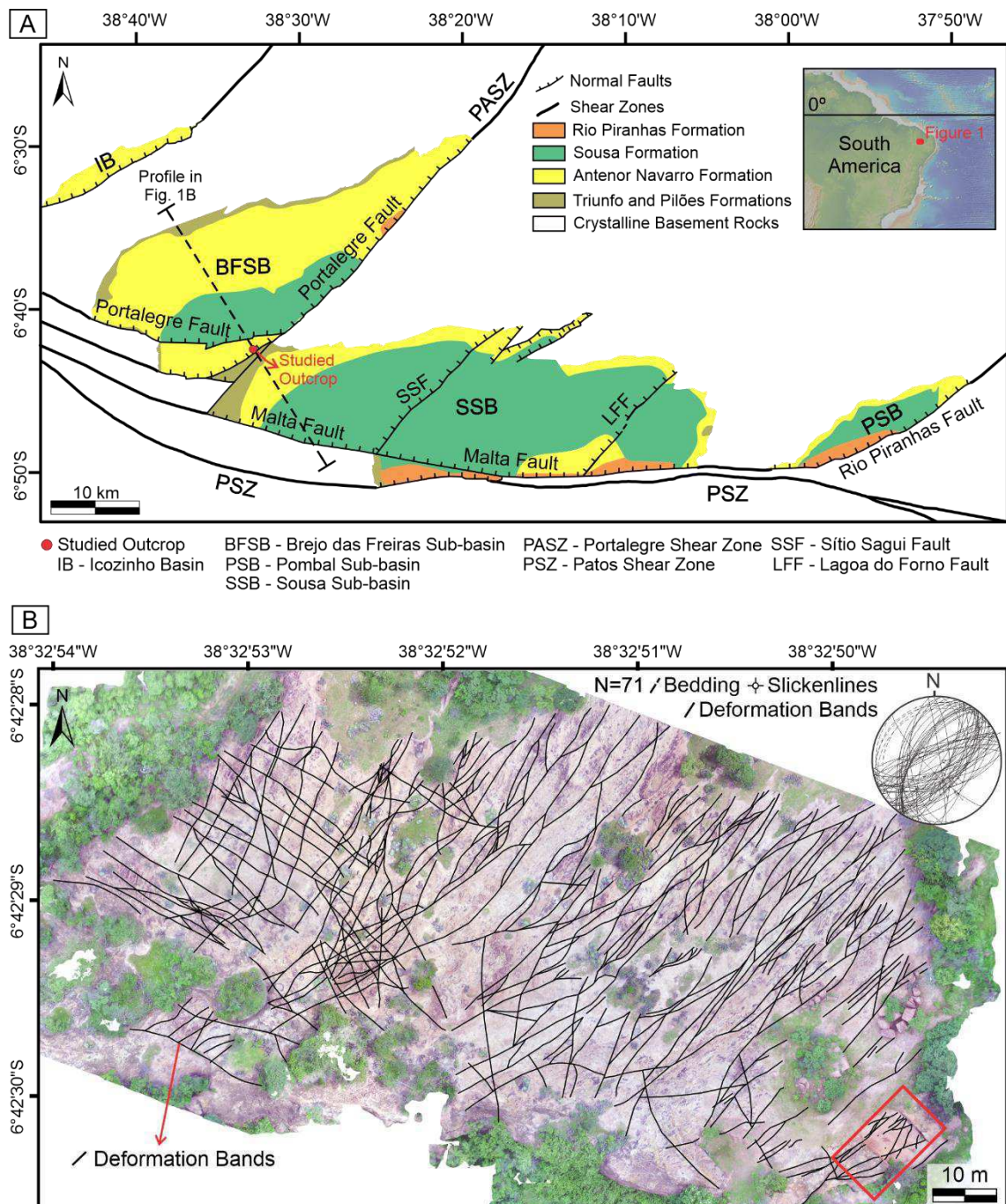


Figure 4.1. (A) Geological map of the Rio do Peixe Basin, showing the NE-SW-striking Portalegre Shear Zone (PASZ), the E-W-striking Patos Shear Zone (PSZ). The main border faults are the E-W-striking Malta Fault (MF), NE-SW-striking Portalegre Fault (PAF), and the NE-SW-striking Rio Piranhas Fault (RPF). The sub-basins are, from west to east are the Brejo das Freiras sub-basin (BFSB), Sousa sub-basin (SBS), and

Pombal sub-basin (PSB) respectively (adapted from Nogueira et al., 2015; Torabi et al., 2021; Vasconcelos et al., 2021). The map also locates the study area of this work (red circle). (B) Unmanned Aerial Vehicle image (UAV) of the outcrop integrated with the main deformation bands clusters mapped in the fault zone (black lines). The studied portion of the fault zone is highlighted in the red square. Stereonet shows the average orientation of deformation bands, as well as slickenlines and sedimentary bedding. N = number of measurements (adapted from Nogueira et al., 2021 and Souza et al., 2022).

4.2. Geological setting

The Rio do Peixe Basin (Figure 4.1A) is an intracontinental basin located in NE Brazil (Françolin et al., 1994; Nogueira et al., 2015). The basin was formed due to brittle reactivation of E-W (Patos) and NE-SW (Portalegre) ductile shear zones of Precambrian ages (Sénant and Popoff, 1991; Françolin et al., 1994; Castro et al., 2007; Nogueira et al., 2015; Nicchio et al., 2022a; Ramos et al., 2022). The reactivation of these shear zones occurred during a regional rifting process associated with the Pangea breakup (Sénant and Popoff, 1991; Françolin et al., 1994; Castro et al., 2007; Nogueira et al., 2015; Nicchio et al., 2022a). These shear zones determined the location and geometry of the three main faults that delimit the Rio do Peixe Basin (Nicchio et al., 2022a; Ramos et al., 2022): the E-W-striking Malta, the NE-SW-striking Portalegre, and the NE-SW-striking Rio Piranhas faults. These faults control three subsidence regions and are represented by semi-grabens: Brejo das Freiras, Sousa, and Pombal sub-basins (Figure 4.1A).

The structural evolution of the Rio do Peixe Basin is characterized by the rift (145-125 Ma) and post-rift phases (80 Ma - present) (Françolin et al., 1994; Castro et al., 2007; Nogueira et al., 2015; Vasconcelos et al., 2021; Ramos et al., 2022). The rift phase is divided into syn-rift I (145-135 Ma) and syn-rift II (135-125 Ma), which is characterized by extensional processes with vertical σ_1 and horizontal σ_3 in the N-S- to NNE-SSE-striking (syn-rift I) and NW-SE (syn-rift II) (Nicchio et al., 2022a). This event was responsible for the development of border faults: Malta, Portalegre, and Pombal, among other internal faults such as Sítio Sagui and Lagoa do Forno (SSF and LFF in Figure 5.A). During the syn-rift phase II, NE-SW-striking deformation bands occur in the damage zone of border faults (Araújo et al., 2018, Nicchio et al., 2022a).

The post-rift phase is known for the mild to moderate tectonic inversion of the basin due to combined stresses from the pushes of the Mid-Atlantic Ridge and the Andes (Nogueira et al., 2015; Vasconcelos et al., 2021). In this phase, σ_1 changed from vertical to horizontal with a maximum compression axis approximate ENE-WSW trending. During this inversion, the basin border faults were partially inverted, preserving the main displacement from the rift phase and locally with reverse displacement. In the sedimentary units, the horizontal compression is characterized by NW-striking (dextral displacement) and N-S-striking (sinistral displacement) conjugated systems of strike-slip faults.

The sedimentary fill of the Rio do Peixe Basin is composed of siliciclastic units (Carvalho et al., 2000; Arai, 2006; Silva et al., 2014) divided into two groups: Santa Helena (Early Devonian) and Rio do Peixe (Early Cretaceous), which are under Precambrian basement rocks. According to Silva et al. (2014), these units are grouped, from base to top, into five stratigraphic units: (1) Pilões Formation, composed of shales and sandstones, related to the deposition of deltaic fans and deltaic fluvial; (2) Triunfo Formation, characterized of fluvial–deltaic white to grey sandstones and conglomerates; (3) Antenor Navarro Formation, formed by fine to conglomerates sandstones and conglomerates, deposited in interlaced fluvial systems and alluvial fans; (4) Sousa Formation, consisting of shales and siltstones interspersed with sandstone, deposited in a lacustrine environment, with localized limestones; (5) Rio Piranhas Formation, composed of fine to conglomeratic sandstones with cross-bedding, deposited in the alluvial environment and fluvial fan in zones proximal to the fault boundary. The Cretaceous units (Antenor Navarro, Sousa, and Rio Piranhas formations) are superimposed on a basal unit dated as Devonian (Pilões and Triunfo) (Roesner et al., 2011; Silva et al., 2014). The present work was performed in conglomeratic sandstones of the Antenor Navarro Formation.

The chosen outcrop for the topological analysis was the target of several previous studies. First, Nogueira et al. (2015, 2021) carried out a broader structural characterization along the fault zone. Later, Bonato et al. (2022) performed a topological analysis on the same broader area as the previously elaborated structural characterization and determined two main domains: fault core domain and damage zone domain. Then, Nicchio et al. (2022b) carried out a more detailed structural characterization, differentiating the deformation bands in two sets of distinct structures

according to the tectonic phase of the basin: the syn-rift system and the post-rift system. Finally, Souza et al. (2022) based on the previously performed structural characterization to analyze the influence of strain bands on fluid flow through numerical simulations. This last study was carried out exactly in the vertical exposure used in our study.

4.3. Methods

We integrate topological and petrophysical data to evaluate the influence of the deformation bands' connectivity on permeability. We used a three-dimensional outcrop exposure, naming the vertical exposure as the XZ plane (Figure 4.2A) and the horizontal exposure as XY plane (Figure 4.2B). We performed the structural mapping from the deformation bands in the field with the support of an Unmanned Aerial Vehicle (UAV) image. We used the MAVIX 2 PRO aircraft, with a flight height of 20 meters and the camera positioned at an angle of 70°, with an image resolution of 0.5 mm/px.

The determination of locations selected for the topological analysis was based on the density of structures and the architectural elements of the fault zone (core and damage zone). We determine these elements in both planes using a profile of the frequency of deformation bands per unit length (P_{10}). To the XZ plane, this profile was demonstrated in a previous study (Souza et al., 2022). In addition, a new P_{10} profile was performed in the XY plane. Then, we defined 23 circular areas with 1 meter diameter, 10 in the XZ plane (Figure 4.2A) and 13 in the XY plane (Figure 4.2B).

The topological analysis in these areas was performed in the QGIS Software using the NetworkGT tool (Nyberg et al., 2018). As input data, we added the shapefiles of the circular areas, composed by mapping the deformation bands, and obtained maps with a grid of 0.25x0.25 for the XZ plane and 0.20x0.20 for the XY plane, as well as data of topology for both planes. Our topological analysis was based on the methodology approached by Sanderson and Nixon (2015), which considers a fracture network formed by components (e.g., nodes, branches, and dimensionless parameters). These authors recognize the three types of nodes shown by Manzocchi (2002) (Figure 4.3A): isolated tips (I-nodes), crossing structures (X-nodes), and abutments or splays (Y-nodes or T-nodes). In addition, Saevik and Nixon (2017) classified the V node (Figure 4.3A), which forms an angle less than or equal to 120°. The branches can be classified into three types (Figure 4.3A): isolated branches (I - I),

branches connected individually with a connection node (I - C), or branches doubly connected with two connection nodes (C - C), where C is X- and Y-node (Sanderson and Nixon, 2015). In this context, Sanderson and Nixon (2015) proposed that for a fracture network consisting of lines, nodes and branches, the parameters P_{20} , P_{21} , and P_{22} classified according to Dershowitz and Herda (1992), can be replaced by their values of equivalent branches, being, respectively, B_{20} , B_{21} and B_{22} (Figure 4.3B).

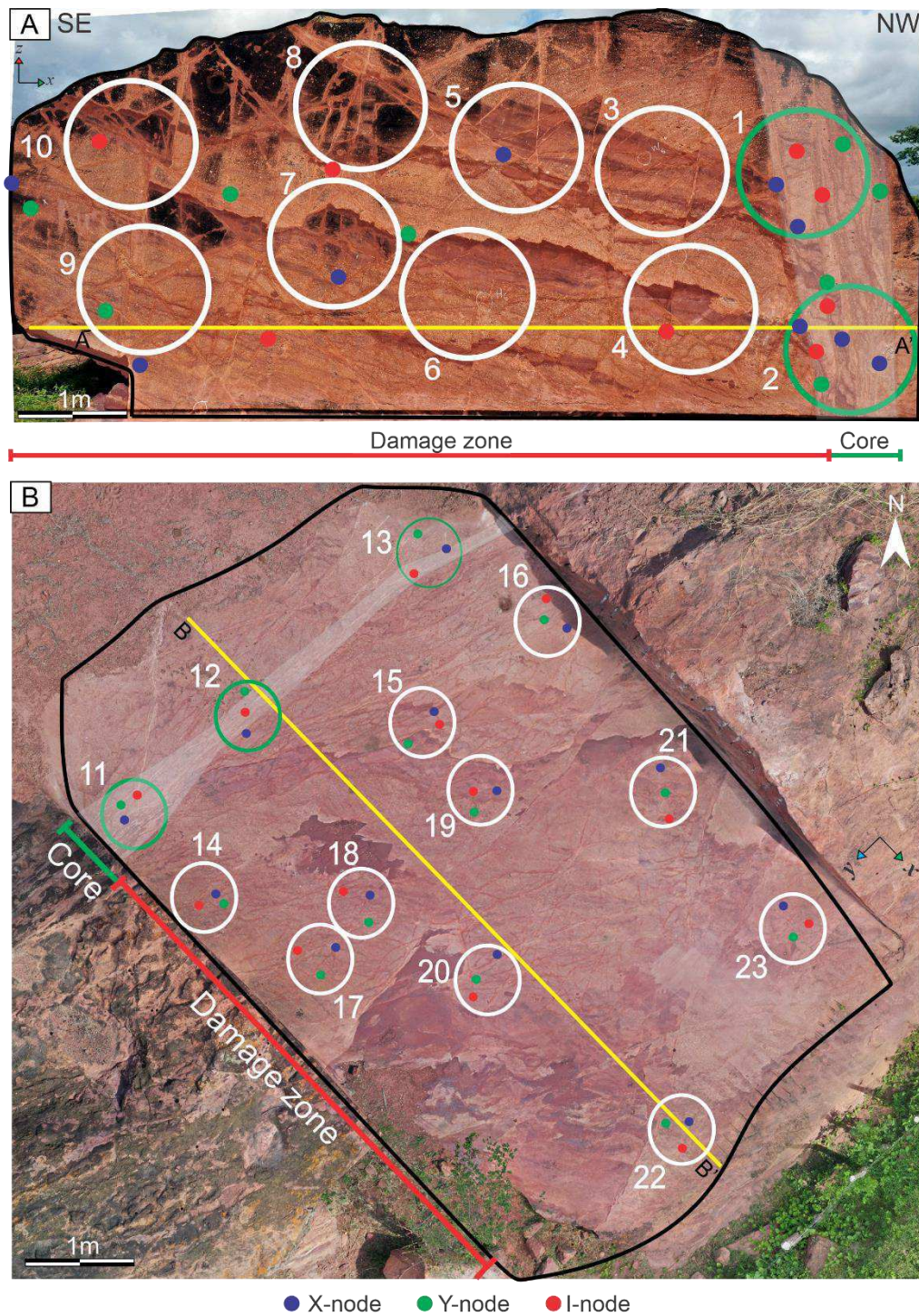
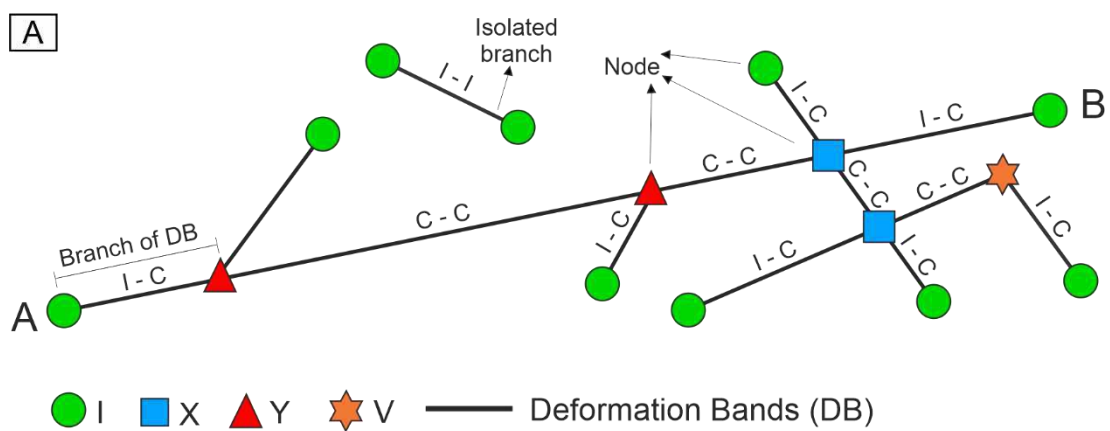


Figure 4.2. (A) Drone image with a view of the XZ plane (wall) and (B) XY plane, showing the location of the circular areas and the boundary of the damage zone (white line) and the fault core (green line). The fault core is highlighted in grey with green circular areas, while the damage zone has red circular areas. The yellow lines represent linear scanlines used for determining the P10 in Figure 4.5. The A-A' segment represent XZ plane scanline and B-B' segment represent XY plane scanline. The smaller circles represent the location of permeability acquisition at each connection: node X (blue), node Y (red) and node I (green).



(B)

		<i>Dimension of Deformation Band</i>			
		0: number	1: length	2: area	3: volume
<i>Dimension of Sampling Region</i>	2: area	B ₂₀ 2-D frequency	B ₂₁ Deformation Band Intensity	B ₂₂ Dimensionless Intensity	

Figure 4.3. (A) Schematic representation of the topology in a deformation band network, showing the types of branches and nodes in the AB segment (adapted from Sanderson and Nixon, 2015; Saevik and Nixon, 2017). (B) Bxy system refers to the terms used for the branches. The line represents the dimension of the sampling region and the columns show the dimension of deformation bands.

The in situ permeability was performed using an air permeability method utilizing the TinyPerm 3 minipermeameter (New England Research, Inc.®). This equipment performs measurements with a range from 10^{-3} to 10 Darcy and 18 mm depth of investigation. We performed the measurements at the deformation band connections

present in circular scanlines (Figures 4.2A and 4.2B). In these regions, three measurements were made at each node, where we performed three measurements at each point and calculated the average. The minipermeameter was positioned at a 90° inclination at each node and programmed with the extrapolated function according to the pressure curve decay was 95% or 120 seconds after the start of the measurement. The equipment was placed horizontally for the Z plane measurement, generating the KY permeability. In contrast, for measurements in the XY plane, the equipment was positioned in the vertical direction, obtaining the Kz permeability.

4.4. Results

4.4.1. Structural Mapping

The structural pattern described in this study is influenced by several previous studies performed in this outcrop (e.g., Nogueira et al., 2015, 2021; Bonato et al., 2022; Nicchio et al., 2022b; Souza et al., 2022). The studied outcrop presents a complex fault zone with deformation bands in a 3D exposure, referent to the XZ plane (wall) and the XY plane (floor) (Figures 4.2A and 4.2B). According to Souza et al. (2022), this fault zone exhibits a fault core and a damage zone. A dextral transtensive fault characterizes the fault core. This fault is a negative flower (Nogueira et al., 2015). Additionally, the fault core record an average thickness of 1 meter. We observed that a higher frequency of parallel deformation bands characterizes the core, referring to an anastomosed pattern. Most of these structures are NE-SW-oriented, dipping to NW (Figures 4.4A and 4.4B). The thicknesses of these core structures are difficult to identify due to the connection between several deformation bands.

A damage zone surrounds the fault core. This damage zone shows an average thickness of 7 meters in the damage zone 1 (d.z.1) and 1 meter in the damage zone 2 (d.z.2) (Figure 4.5). Several deformation bands with centimetric and millimetric displacements characterize the damage zone. The deformation bands in the damage zone present a complex behavior (rhombohedral) with a high variability of direction and dip, causing several crossings. The thickness of these structures varies from a few mm to several cm. Overall, the deformation bands are predominantly NE-SW-striking, and secondarily NW-SE-striking, N-S-striking, and E-W-striking (Stereonet in Figure 4.1B). Two fault systems occur in the study area, a syn-rift and a post-rift (Figure 4.4) (Nicchio et al., 2022b). The syn-rift system presents dextral transtensive kinematics, interpreted

by Nicchio et al. (2022b) as synthetic and antithetic faults concerning the main border fault (Portalegre Fault; Figure 4.1A). This system is crosscut by post-rift faults, which form a conjugate strike-slip fault system, with NW-SE-striking dextral and NNE-SSW-striking sinistral subvertical faults (Nicchio et al., 2022b).

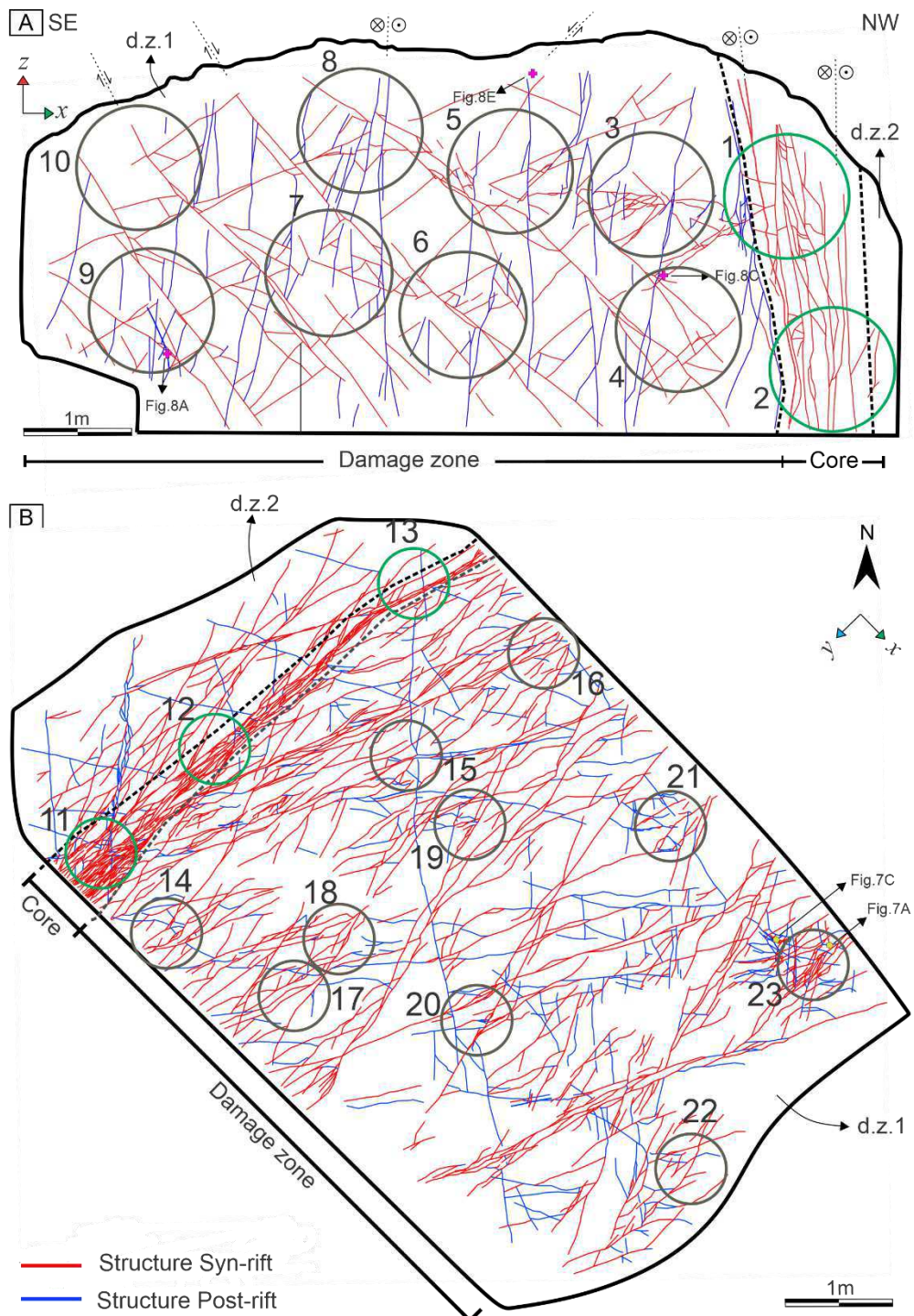


Figure 4.4. Characterization of the two fault systems present in the (A) XZ Plane and (B) XY Plane of the Melancias Outcrop. The red lines represent the structures formed

by the Syn-rift System and the blue lines highlight the structures of the Post-rift System. The nodes of Figure 4.7 and Figure 4.8 are located by the black arrows.

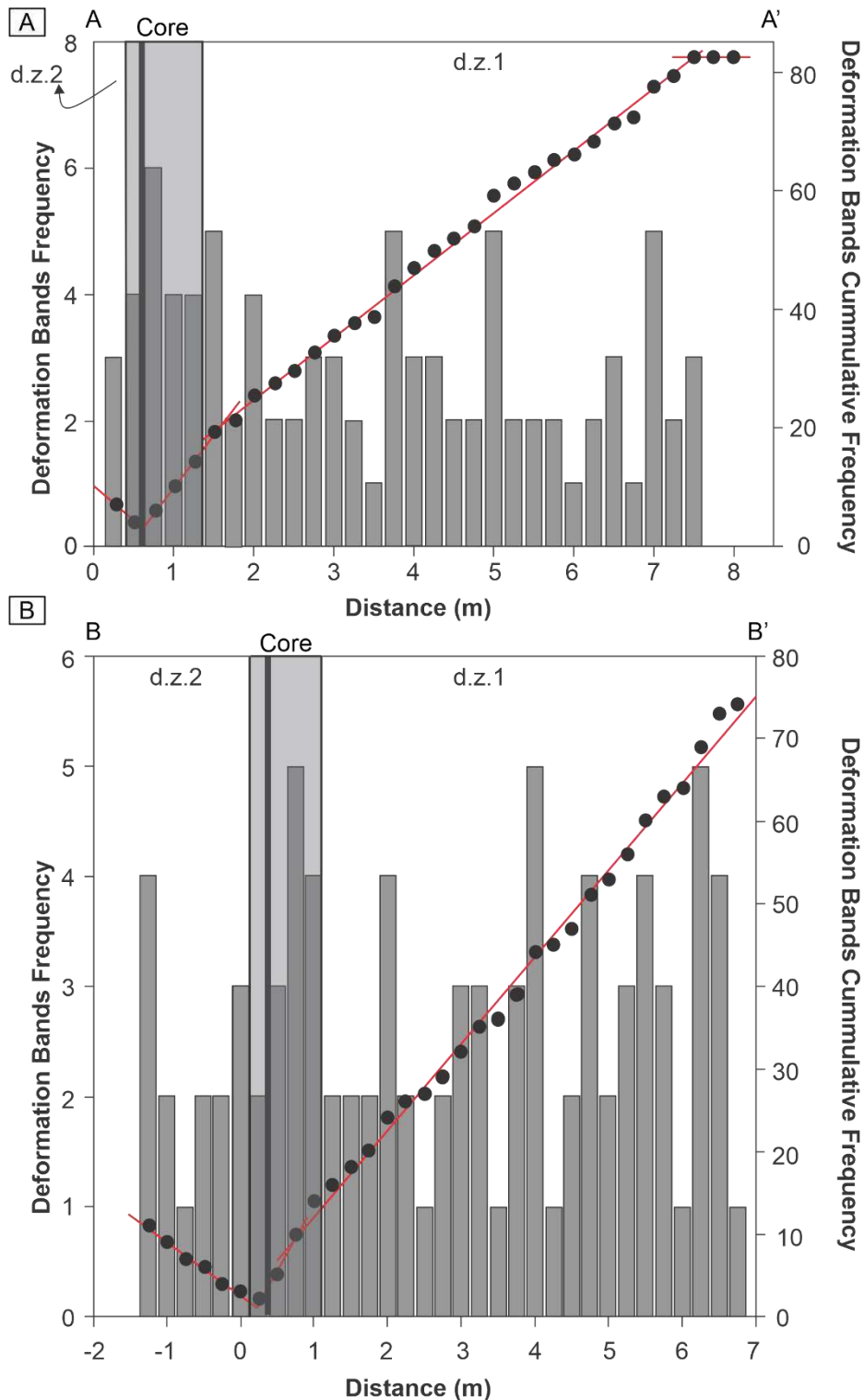


Figure 4.5. Graph of frequency and cumulative frequency of deformation bands recorded in the scanline (yellow line in Fig. 4.4) the XZ plane (Figura 4.4A) (adapted

from Souza et al. 2022) and the XY plane (Figure 4.4B). d.z.1 = damage zone 1; z.d.2 = damage zone 2.

4.4.2. Topological analysis

The most common nodes observed in the topological analysis performed on the wall and floor of the outcrop (XY and XZ planes, respectively) are X- > Y- > I-nodes. In addition, we recorded new types of connections (Figure 4.6). These nodes are formed of five (Figure 4.7) and six (Figure 4.8) branches intersecting the same point, which we defined as H and W, respectively.

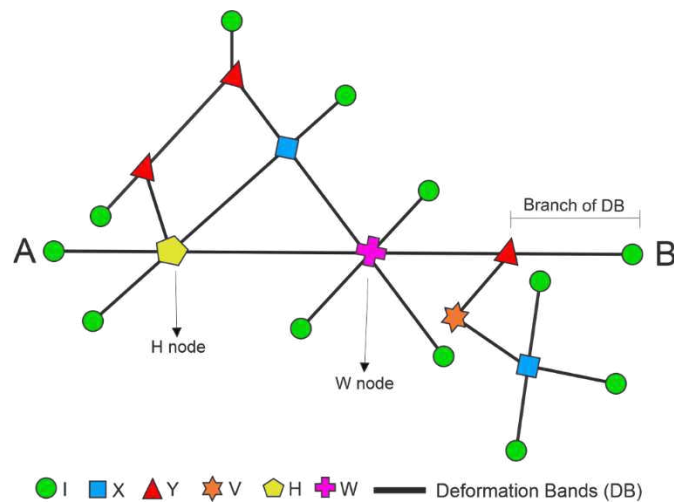


Figure 4.6. Schematic model for a deformation band network showing the types of nodes previously discussed (Sanderson and Nixon, 2015; Saevik and Nixon, 2017) and the new nodes found in this study (H and W nodes).

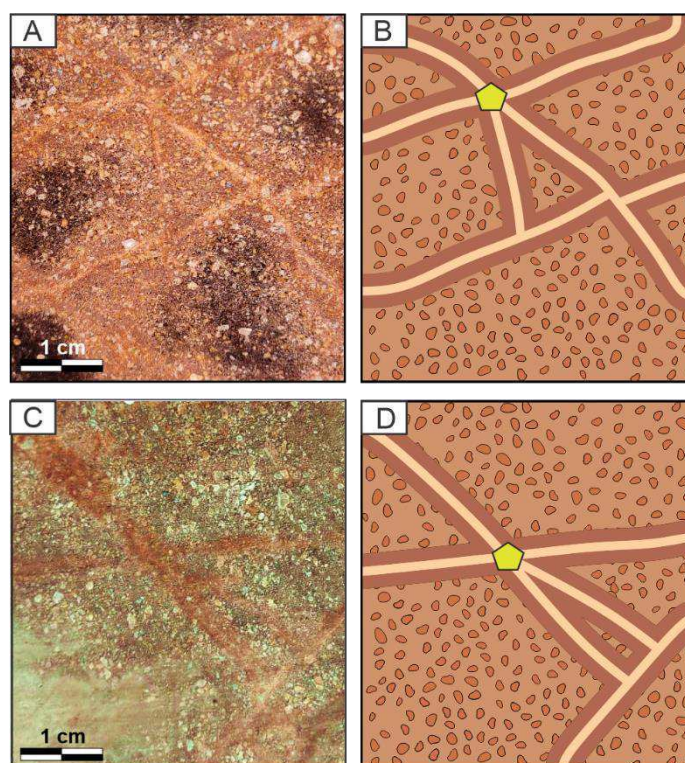


Figure 4.7. Characterization of the intersection of five deformation band branches at the same point (H-node). (A, C) Outcrop wall images and (B, D) schematic drawing showing the H-node, where is observed the intersection of five branches of deformation bands at the same point. The location of the photographed points can be seen in Figure 4.4.

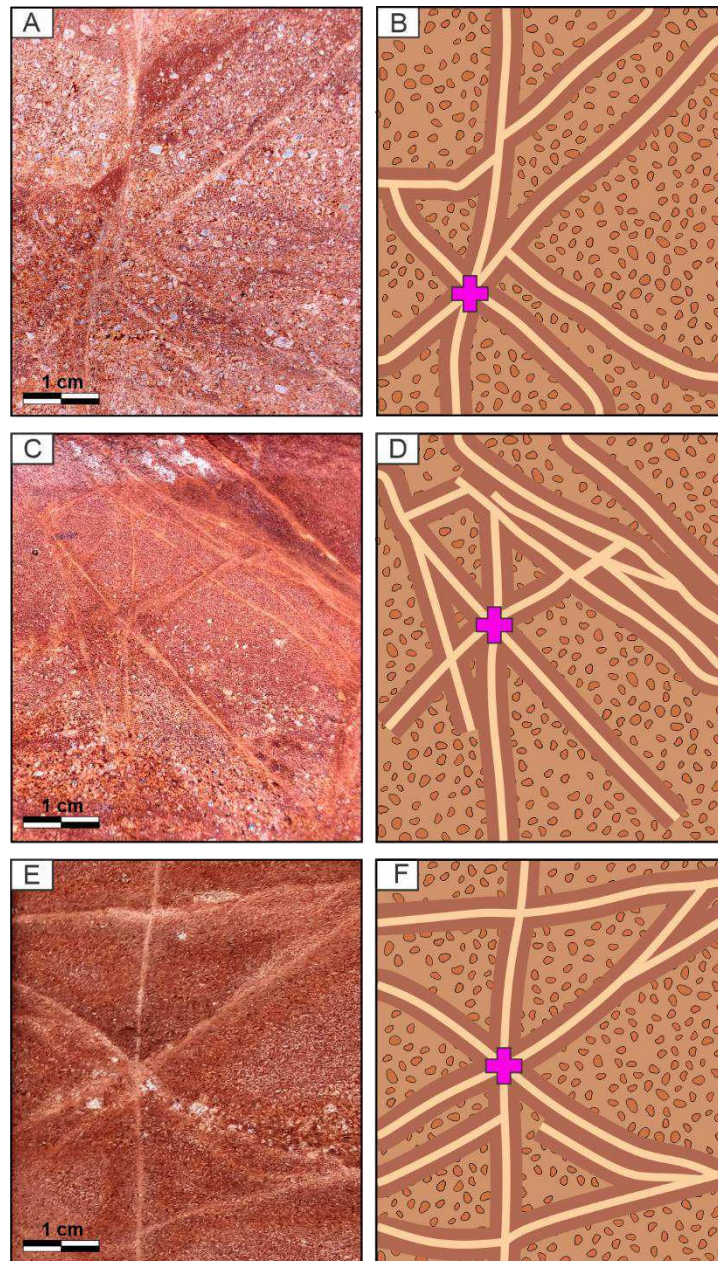


Figure 4.8. Characterization of the intersection of six deformation band branches at the same point (W-node). (A, C, E) The portion of the outcrop without interpretation, and (B, D, F) schematic drawing showing the W-nodes. The location of A, C, and E can be seen in Figure 4.4.

The fault core has higher values than the damage zone for the topological parameters: Number of nodes (N_N), Number of branches (N_B), Connecting node frequency (N_C), Dimensionless intensity (B_{20}), Isolated branches (I-I), Partly connected branches (I-C), and Doubly connected branches (C-C) (Table 4.1). The core presents three times more connections in the XY plane than the XZ plane for the parameters destined for the amount of X-, Y-, and I- node; N_N , N_B , and Freq. N_C ; B_{20} ; C-C and I-C.

In contrast, in the damage zone, there are no significant variations for these parameters (Table 4.1).

The connectivity proportion of nodes varies along the fault zone (core and damage zone). In the core, 9%, 13%, and 78% correspond to the X-, I-, and Y-nodes, respectively. In the damage zone, the proportion of X-, I- and Y-nodes are 18%, 15%, and 67%, respectively (Figure 4.9). In addition, we analyzed the topological maps of the number of connections for the XZ plane (Figure 4.10A) and XY plane (Figure 4.10B). In the XZ plane, we note the oscillation from low to medium values in the core and high to medium values in the damage zone (Figure 4.10A). In the XY plane, the number of connections presents higher values in the core, being reduced in the damage zone as it moves away from the core. The damage zone has some regions with average values, except for a small area with the same intensity as the core (Figure 4.10B), where we observed H - and W - nodes.

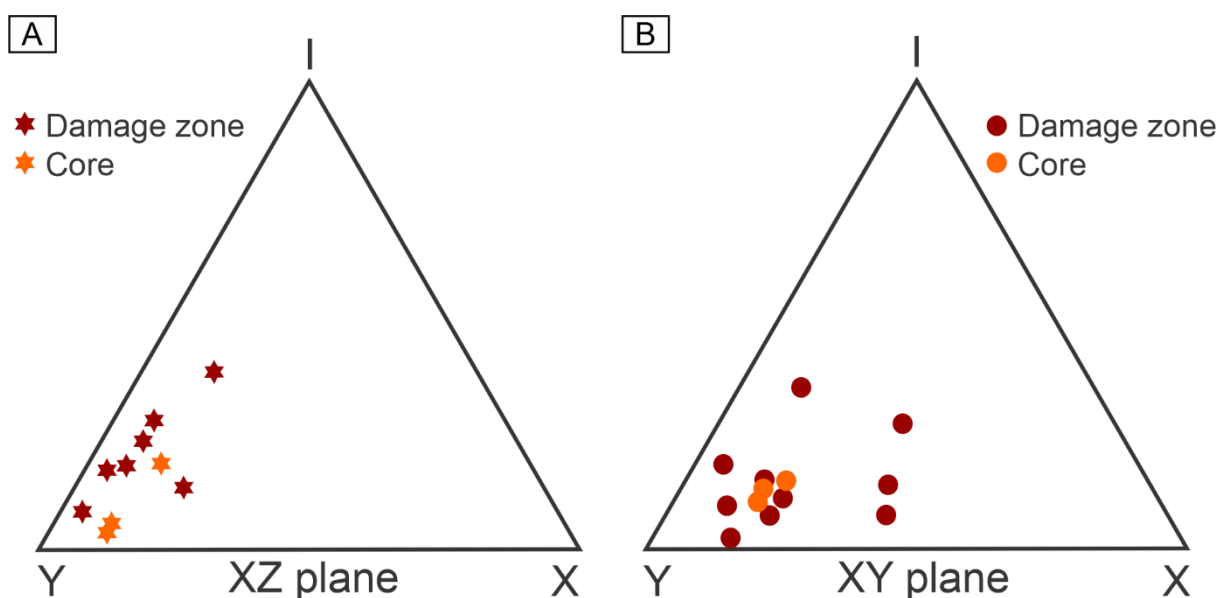


Figure 4.9. Ternary diagram showing the proportion of nodes in the architectural elements of the fault zone (core and damage zone) to the (A) XZ plane and (B) XY plane. The symbols in red are referring to the data of the circular areas disposed of in the damage zone and the orange symbols represent the fault core data.

Regarding the branches, the topological maps numbers of branches for the XZ plane (Figure 4.11A) and XY plane (Figure 4.11B) showed behavior similar to that analyzed in the maps of the number of connections (Figure 4.10). In the XZ plane, the intensity of branches varies from medium to high in the damage zone, with lower values

in the fault core (Figure 4.11A). In the XY plane, the intensity of branches is higher in the core and decreases in the damage zone when moving away from the fault core, with regions of moderate values and locally a region with the same value as the core (Figure 4.11B). Furthermore, the deformation bands present approximately six times more doubly connected branches (C-C) than partly connected branches (I – C) (Table 4.1). The core in the XY plane has approximately 3.8 times more C-C branches than the XZ plane. In addition, the fault core has no I-C branches in the XZ plane. Similarly, the damage zone has around five times more C-C branches than I-C branches (Table 4.1). In both planes, the damage zone has similar values of C-C branches. However, similarly to the fault core, it does not present any C-I branch in the XZ plane.

The circular scanline data indicate Y-nodes predominance (Figures 4.12 and 4.13; Tables 4.2 and 4.3). However, there are variations along the architectural elements of the fault zone. For example, in the core, both planes are characterized by the domain of Y-nodes and secondarily of I-and X-nodes (scanlines 1 and 2 of Figure 4.12; scanlines 11, 12 and 13 of Figure 4.13). In contrast, in the damage zone, a divergent connection pattern is reported with Y-nodes predominating in the XZ plane, followed by X- and I-nodes (Table 4.2), while in the XY plane, the connection pattern changes as areas move away from the core. In the areas close to the core, the pattern of nodes is $Y > I > X$ (Scanlines 14, 15 and 16 of Figure 4.13), and in the most distant areas, the pattern is $Y > X > I$ (Scanlines 21 and 23 of Figure 4.13).

Finally, we related the parameter number of branches (N_B) with the dimensionless intensity (B_{20}) (Tables 4.2 and 4.3). In highly connected and branched areas, higher values of B_{20} occur. For instance, in the fault core of the XY plane (e.g., areas 1 and 2 of Table 4.3 and Figure 4.2B) and of the damage zone in the XY plane (e.g., area 13 of Table 4.3 and Figure 4.2B), as well as in the damage zone of the XZ plane (e.g., areas 3, 5 and 7 of Table 4.2 and Figure 4.2A). In addition, the circular areas with a greater number of nodes (N_N) and a higher frequency of Y-nodes also present a greater quantity of doubly connected branches (C-C). For example, the core in the XY plane (e.g., areas 1 and 2 of Table 4.3 and Figure 4.2B), the damage zone in the XY plane (e.g., areas 10, 11, and 13 of Table 4.3 and Figure 4.2B) and the damage zone in the XZ plane (e.g., areas 3, 5, 7, and 8 of Table 4.2 and figure 4.2A).

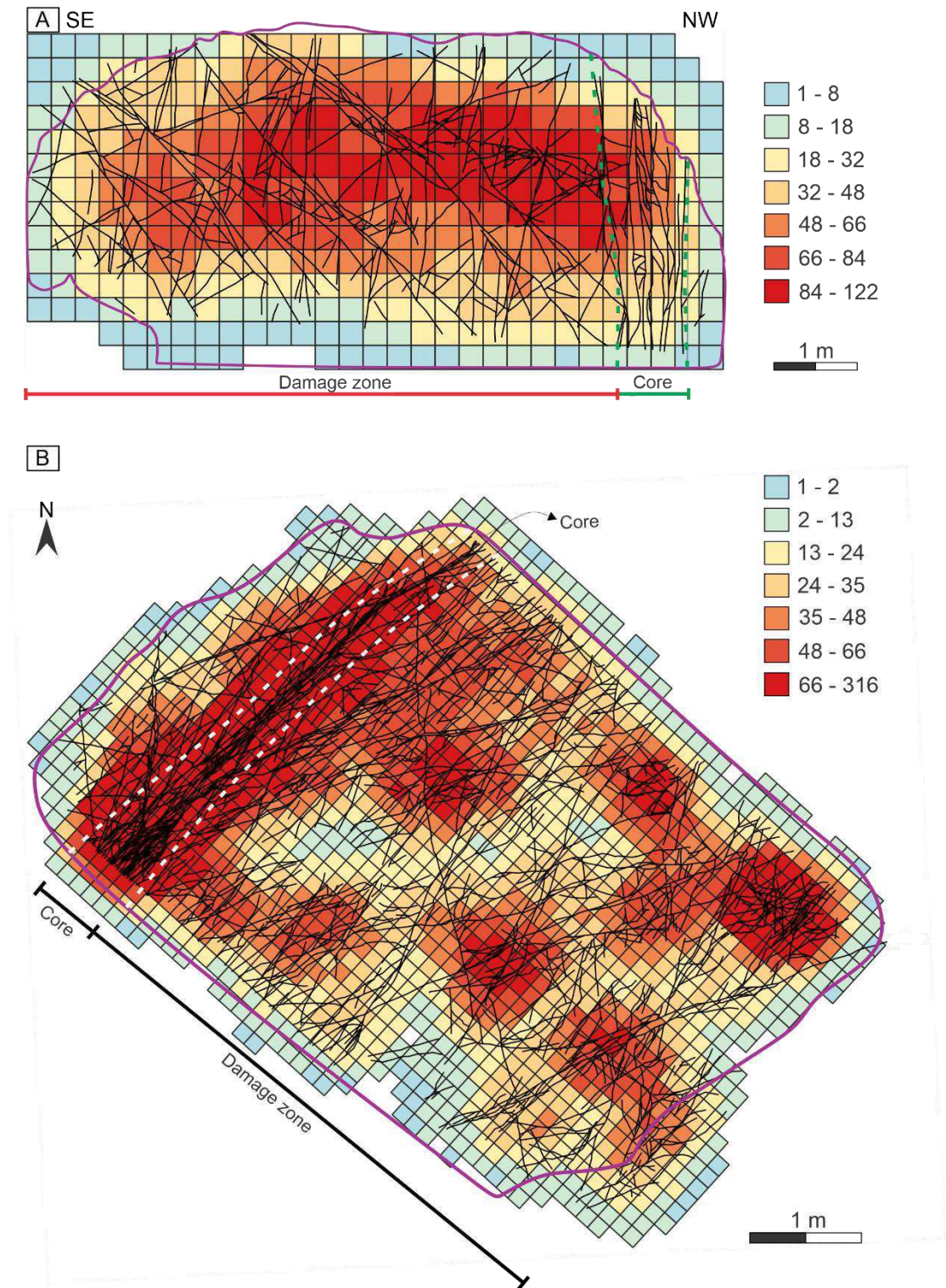


Figure 4.10. Topological map with the number of connections for the (A) XZ plane (wall) and (B) XY plane (floor) of the outcrop. The purple outline limits the analyzed area and the reddish color regions represent a higher number of connections. The green dashed line represents the fault core in the XZ plane and the white dashed line represents the fault core in the XY plane.

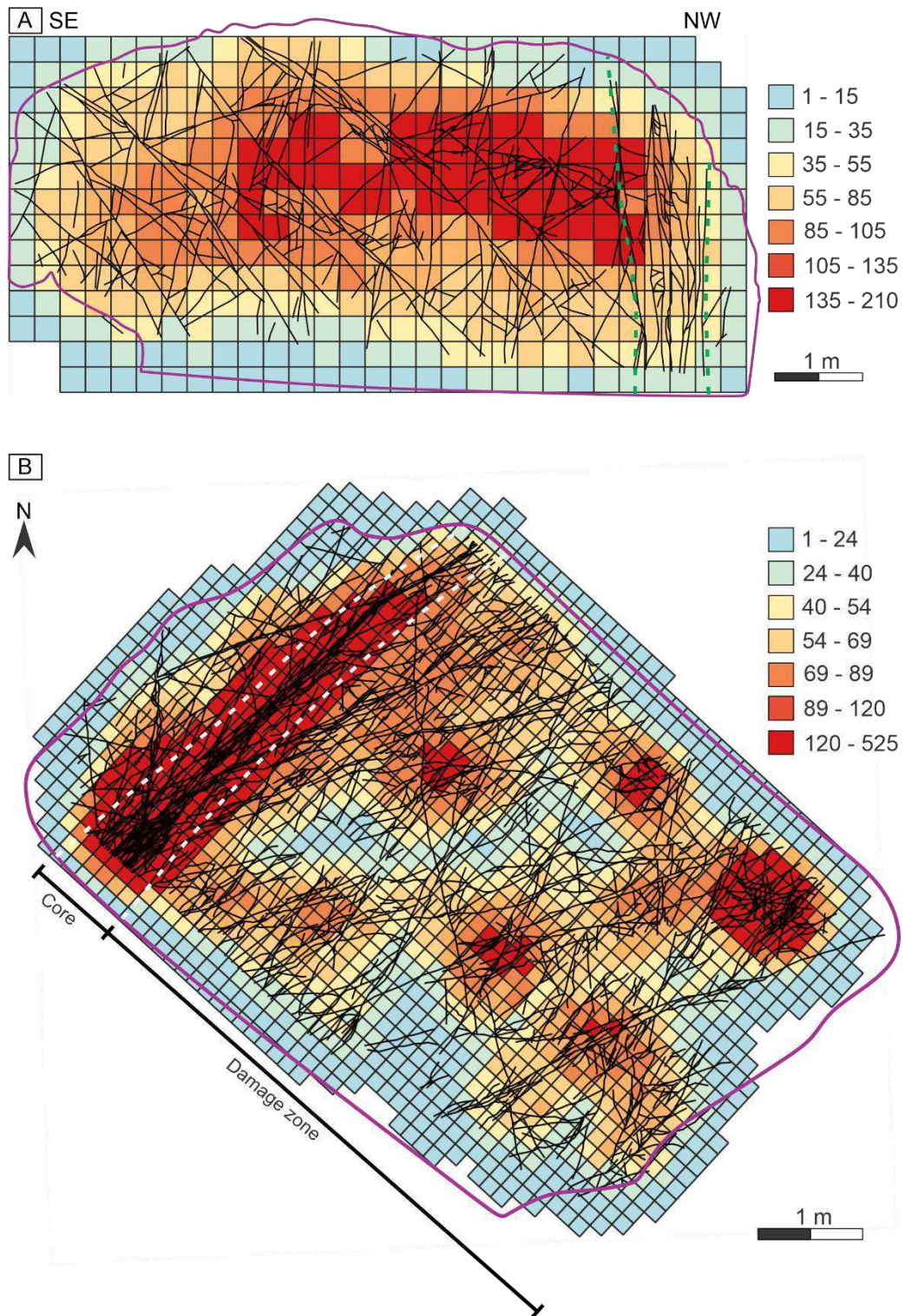


Figure 4.11. Topological map of the number of branches for the XZ plane (A) and XY plane (B) of the studied outcrop. The regions with darker coloration present a greater number of branches. The purple outline limits the analyzed area and the reddish color regions represent a higher number of branches. The green dashed line represents the

fault core in the XZ plane and the white dashed line represents the fault core in the XY Plane.

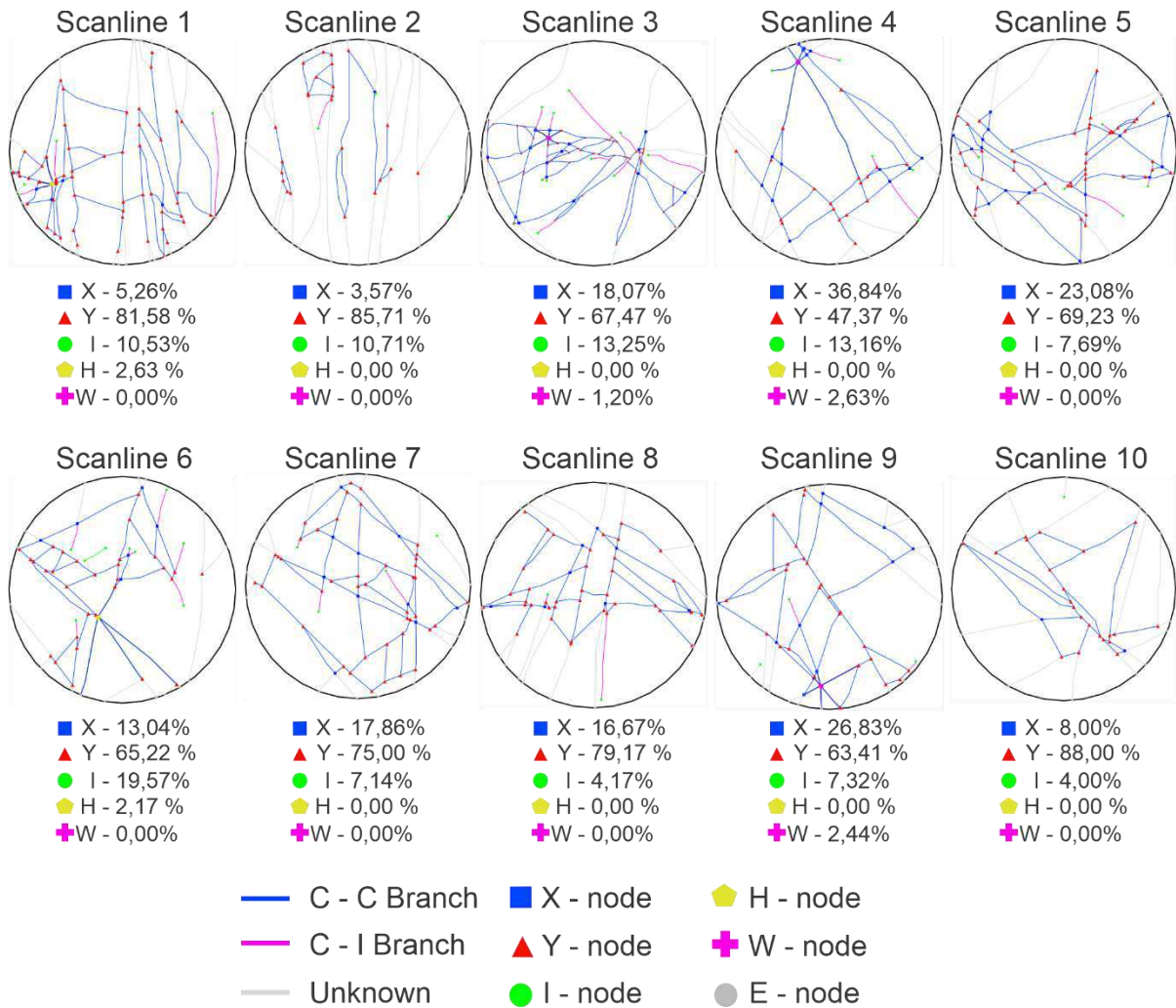


Figure 4.12. Detail of the topology for the XZ Plane (wall) circular scanlines, showing the percentage of different types of nodes for each area and the branches formed by the connections. The location of scanlines areas is in Figure 4.2A.

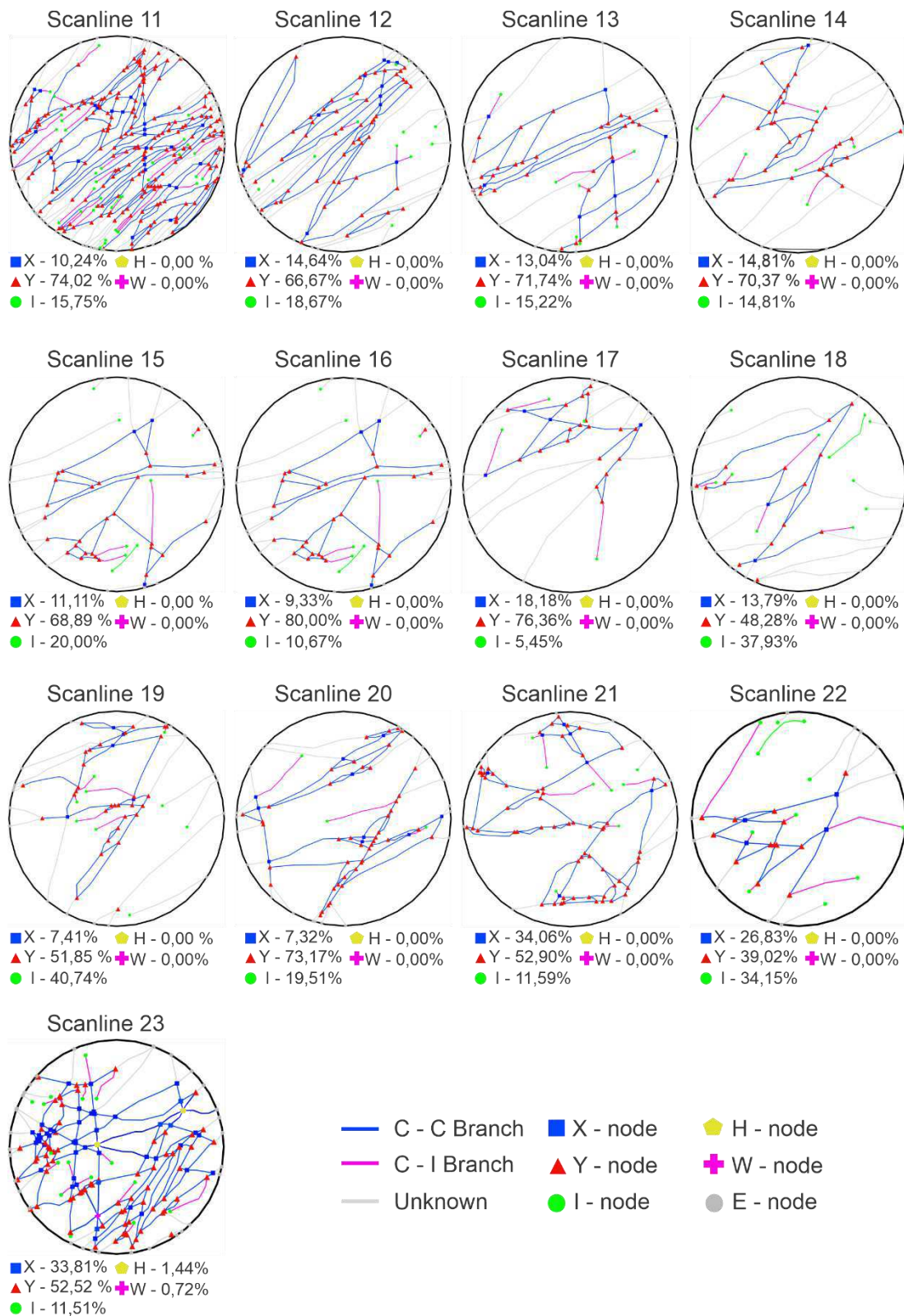


Figure 4.13. Topology of individual areas of the XY plane (floor) with the percentage of each type of connection and the branch formed by the connections. The location of scanlines areas is in Figure 4.2B.

Table 4.1. Average values of topological parameters between the XY (wall) and XZ (floor) planes for the core and damage zone. Analyzed parameters: X-Node, Y-Node, I-Node, Number of nodes (N_N), Number of branches (N_B), Connecting node frequency (N_C), Dimensionless intensity (B_{20}), Isolated branches (I-I), Partly connected branches (I-C), Doubly connected branches (C-C).

Parameters	Core			Damage zone		
	XY Plane	XZ Plane	Total	XY Plane	XZ Plane	Total
X	14	2	16	9	10	19
Y	90	28	118	33	35	68
I	20	4	24	9	5	14
N_N	125	33	158	52	50	102
N_B	174	46	220	73	75	148
Freq. N_C	134	37	171	55	57	112
B_{20}	223	59	282	94	96	190
C - C	152	40	192	57	67	124
C - I	26	0	26	11	0	11

Table 4.2. Topological parameters of XZ plane (wall) circular scanlines. Analyzed parameters: X-Node, Y-Node, I-Node, Number of nodes (N_N), Number of branches (N_B), Connecting node frequency (N_C), Dimensionless intensity (B_{20}), Isolated branches (I-I), Partly connected branches (I-C), Doubly connected branches (C-C).

	Sample	X	Y	I	N_N	N_B	Freq. N_C	B_{20}	C-C	C-I
Core	1	2	31	4	37	53	42	67	48	4
	2	1	24	3	28	40	32	51	32	8
Damage zone	3	15	56	11	82	120	91	153	105	12
	4	14	18	5	37	58	41	74	49	6
	5	15	45	5	65	100	77	128	94	6
	6	6	30	9	45	62	46	79	50	9
	7	10	42	4	56	85	67	109	81	4
	8	8	38	2	48	74	59	95	69	5
	9	11	26	3	40	63	47	80	55	5
	10	2	22	1	25	38	31	48	36	2

Table 4.3. Topological parameters of XY plane (floor) individual areas. Analyzed parameters: X-Node, Y-Node, I-Node, Number of nodes (N_N), Number of branches (N_B), Connecting node frequency (N_C), Dimensionless intensity (B_{20}), Isolated branches (I-I), Partly connected branches (I-C), Doubly connected branches (C-C).

	Sample	X	Y	I	N_N	N_B	Freq. N_C	B_{20}	C-C	C-I
Core	11	26	188	40	254	354	274	453	309	43
	12	11	50	14	75	104	78	133	91	12
	13	6	33	7	46	65	50	83	56	10
Damage zone	1	1	34	6	41	56	45	72	44	12
	15	3	30	8	41	55	42	70	5	11
	16	11	16	14	41	53	42	70	5	11
	17	4	19	4	27	39	29	49	31	8
	18	2	14	11	27	31	20	39	19	10
	19	5	31	9	45	61	46	78	53	8
	20	10	42	3	55	85	67	108	79	6
	21	7	60	8	75	108	86	138	97	11
	22	4	14	11	29	35	23	44	22	10
	23	47	73	16	136	212	154	271	183	22

4.4.3. Permeability versus node type

We analyze the impact of different connections of deformation bands on permeability along the fault zone. Within the fault core, the X-node always presents the lowest permeability values, followed by Y- and I-nodes, with one order of magnitude (Figure 4.14). In the XZ plane, the X-, Y-, and I-nodes showed the same order of magnitude and the following mean values: 1.0 mD, 1.71 mD, and 4.07 mD, respectively. However, the XY plane recorded higher average values: 1.32 mD for the X-node, 13.21 mD for the Y-node and 29.68 mD for the I-node. In the XZ plane, the permeability is smaller in X-node, followed by Y- and I-nodes, with mean values of 2.08 mD, 6.87 mD, and 72.35 mD, respectively (Figure 4.14). For the XY plane, the permeability shows the Y-node with the smallest average, followed by X- and I-nodes, with respective average values of 8.43 mD, 10.64 mD, and 36.60 mD.

Furthermore, we reported that the permeability property demonstrates an anisotropic behavior along the outcrop. The permeability in the XY plane is slightly greater when compared to the XZ plane. Therefore, the vertical permeability (K_z) is greater than the horizontal permeability (K_y).

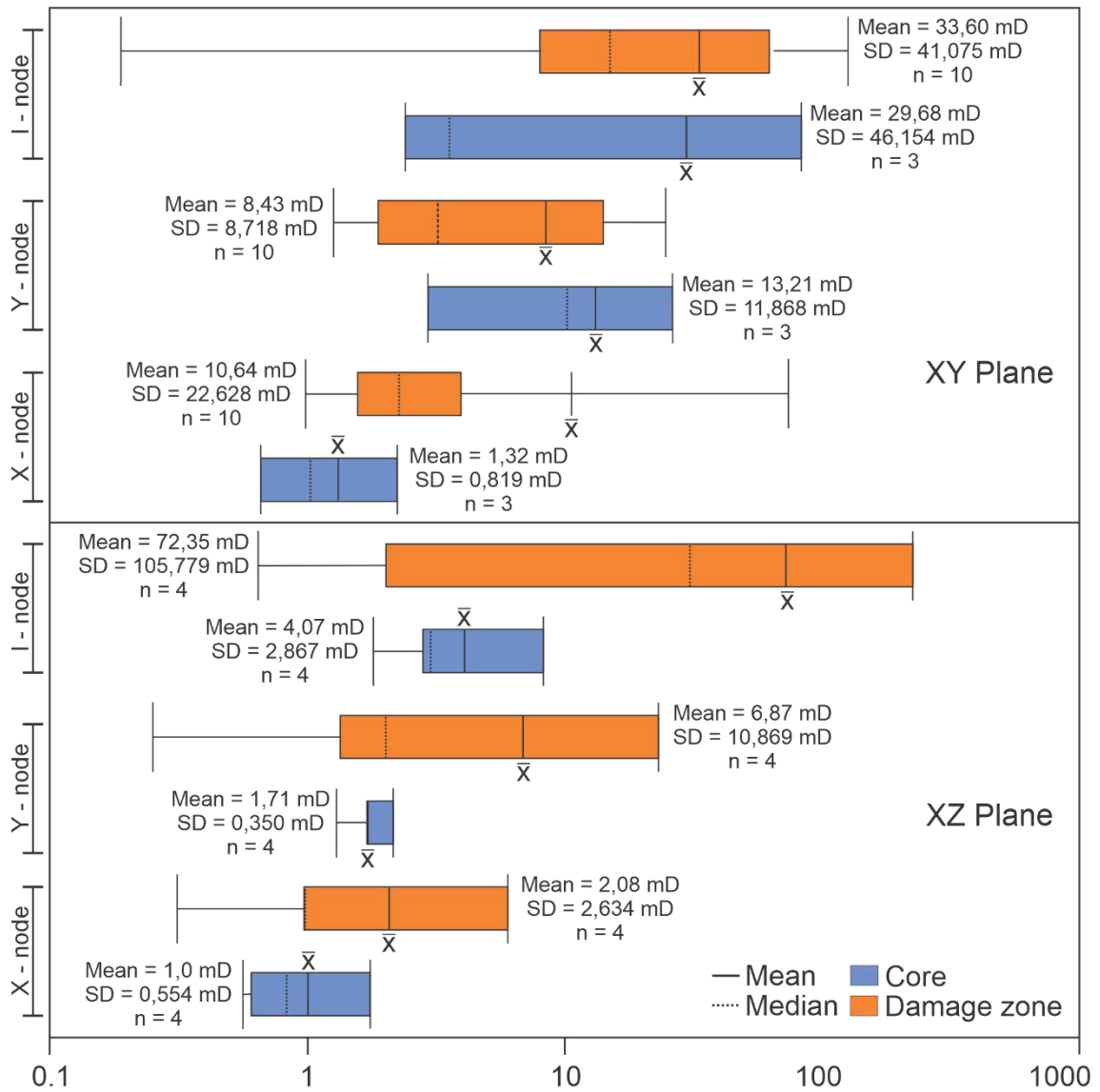


Figure 4.14. Permeability graph of I-, Y-, and X-nodes present in the XZ plane (wall) and XY plane (floor). Orange rectangles show damage zone data. Blue rectangles represent core values. The black lines inside the rectangle refer to the median. The upper and lower black lines mean the maximum and minimum permeability values, respectively.

4.5. Discussions

4.5.1. Implications of tectonics from the Rio do Peixe Basin in topology analysis

The topological analysis was initially developed to analyze the fracture relationship (Manzocchi, 2002), considering X-, Y-, and I-nodes for a fractures network. Posteriorly, Saevik and Nixon (2018) introduced a new node that influenced the tortuosity rock, defined V-node. Both studies performed the classification of the nodes applied to fractures. On the other hand, Gjestland (2020) and Bonato et al. (2022) applied the topology in deformation bands. For example, Gjestland (2020) characterized intersection and wall damage zones. Bonato et al. (2022) evaluated the influence of trace length and deformation band orientation, analyzing if these structures would act as barriers or conduits for the flow of fluids in porous media. In this research, applied to deformation band, was verified the existence of two new node types: H and W.

The previously discussed connections (Manzocchi, 2002; Saevik and Nixon, 2018) and the new nodes found in this study can be formed from one or more fault systems. The X-, Y-, and I-nodes occur in a single fault system, in which the crossing of faults forms the X-node, the Y-node appears from the fault termination on another fault, and the I-node is formed by termination of fault. In contrast, the H- and W-nodes are formed when two fault systems crosscut each other (Figure 4.15). In this study, syn-rift structures are crosscut by post-rift structures (Nogueira et al., 2015; Nicchio et al., 2022b). Based on these previous studies, we interprets that these new components were developed from a sin-rift fault system and a post-rift fault system (e.g., Nogueira et al., 2015, 2021; Souza et al., 2022; Nicchio et al., 2022b). In this context, we propose that the W-node occurs when antithetic and synthetic faults (syn-rift system) are crosscut by sub-vertical post-rift faults (Figure 5.15). On the other hand, the H-node occurs when the dextral and sinistral faults does not crosscut the intersection of synthetic and antithetic faults (Figure 5.15). We suggest that the absence of crosscutting relation between faults for H-node formation is due to increased rock strength due to deformation band clustering development (Pontes et al., 2019). In these situations, the greater the density of deformation bands, the greater the mechanical strength of the rock. Therefore, in sedimentary basins with multiphase reactivation, the occurrence of more H and W connections must be more frequently.

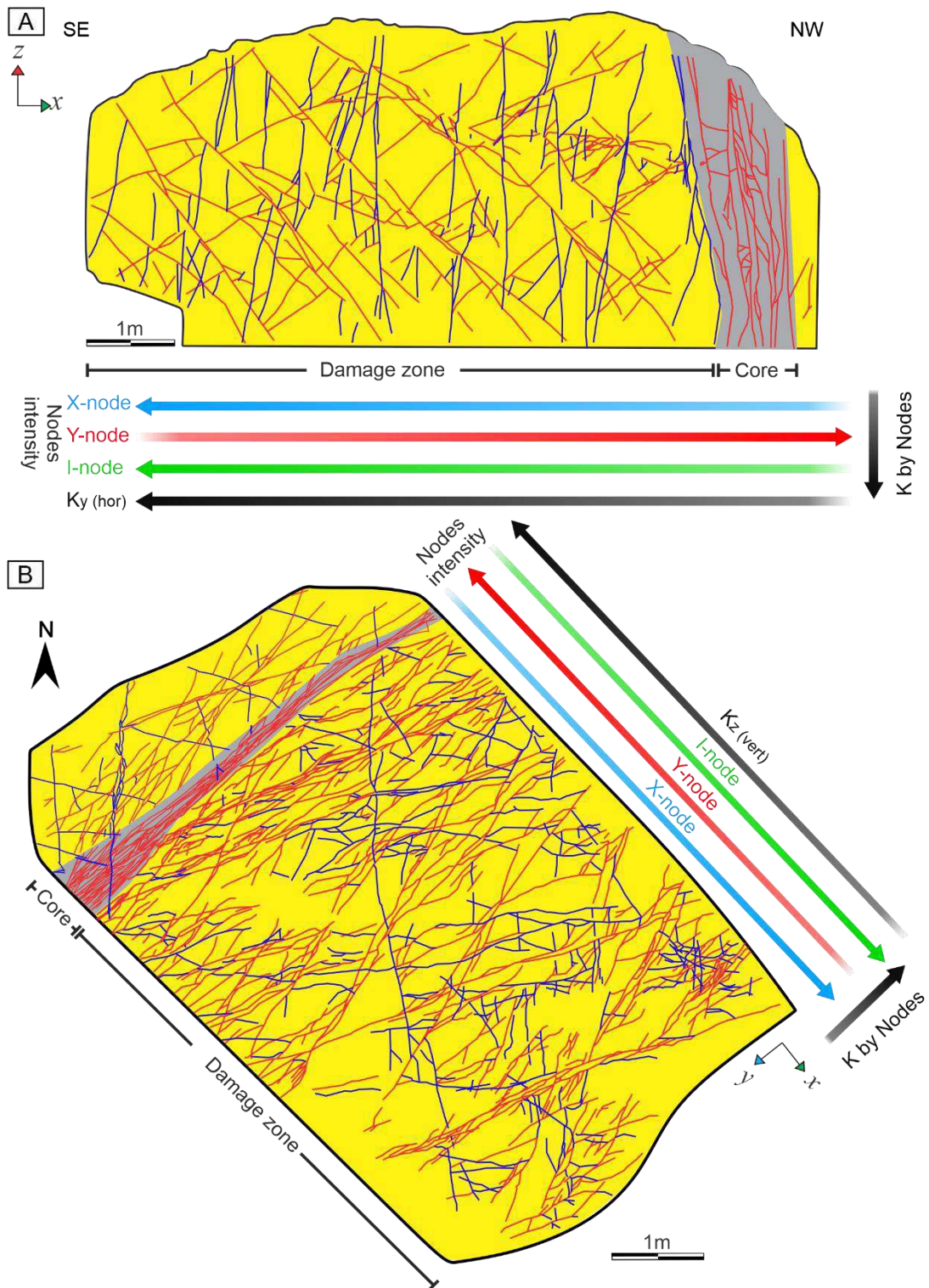


Figure 4.15. General schematic model of the 3D exposure of the outcrop showing (i) the predominance of Y nodes in both planes (XZ and XY); (ii) the intersection between syn-rift and post-rift fault systems; (iii) permeability variation in both planes for each type of connection.

4.5.2. Structural characterization of deformation bands: topological analysis

Several studies were performed to characterize the connections between fractures through topological analysis. For example, Manzocchi (2002) demonstrated that X-nodes rarely occur (e.g., joints, fractures, and faults). Additionally, there are structural patterns in which the I-node predominates over to the Y-node (Manzocchi, 2002; Morley and Nixon, 2016). However, the applied topology for deformation bands shows that the connection between these structures is dominated by Y-nodes (Gjesteland, 2020; Vagle, 2020). These authors proposed that the deformation bands are more prone to bifurcation and less to the structures crossing, forming more adjacent bands and fewer transverse bands, promoting a high proportion of Y-nodes and a low proportion of X-nodes. In addition, these authors suggest that I-nodes are commonly associated with short and partially connected bands.

In our study, the three-dimensional connectivity of deformation bands showed a high proportion of Y-nodes and doubly connected branches (C-C) along the fault zone. We noticed that the fault core predominates of Y-nodes (78%) in detriment to I- and X-nodes (13 and 9 %, respectively). Regarding the damage zone, there is the predominance of Y-nodes (67%) to the detriment of X- and I- nodes (18 and 15%, respectively). We interpret that this preferred pattern of development of Y-nodes in deformation bands occurs due to the frequently three-dimensionally rhombohedral pattern of these structures along fault zones (Nogueira et al., 2021; Bonato et al., 2022; Oliveira et al., 2022; Souza et al., 2022). However, we suggest that the proximity of the fault core, although still the present dominance of Y-nodes, tends to make this pattern less rhombohedral and promote the secondary development of I-nodes to the detriment of X- nodes. In contrast, the X-nodes are most common as move away from the fault core due to the crosscut by several deformation bands. Therefore, according to our results, the Y- and I-nodes also developed due to the clustering process of deformation bands present in the fault core of deformation band fault zones, while the X-nodes are developed due to the crosscut by several deformation bands.

Additionally, we observed that the number of connections is directly proportional to the thickness of the core of the XZ plane (Figure 4.9). We suggest that this is due to the intensity of deformation in the fault core.

4.5.3. Implication of topological analysis for reservoirs

The deformation bands commonly affect the petrophysical properties of the host rocks (Ballas et al., 2015; Fossen et al., 2017; Nogueira et al., 2021) and control the fluid flow behavior in the reservoir (Awdal et al., 2020; Souza et al., 2022; Stohler et al., 2022). Furthermore, the connectivity of these structures can be a controlling factor in the flow pattern of the reservoir (Fossen and Bale, 2007; Rotevatn et al., 2013; Souza et al., 2022). According to some studies, the high connectivity of deformation bands can baffle fluid (Fossen et al., 2005; Fossen and Bale, 2007; Gjesteland, 2020; Souza et al., 2022). In our case, the higher connectivity is mainly associated with the deformation bands' anastomosing arrangement in the fault core. A recent study in the same outcrop suggests that the anastomosing arrangement of the deformation bands in the fault core increases the sealing potential (Souza et al., 2022). The same study indicates that the fluid conduit behavior also depends on the flow direction. We suggest that the vertical fluid flow, parallel to the deformation bands of the fault core, will be more conducive than horizontal fluid flow because the deformation bands' connections are more intense in the horizontal plane (Figure 4.11).

Additionally, Souza et al. (2022) evaluated the influence deformation bands on fluid flow with 2D numerical simulation. These authors highlighted that the anastomosing behavior and the intersection between the deformation bands with varied dips affect the fluid flow. Furthermore, when the fluid flow is parallel to the deformation bands, these structures act as fluid conduits along the length of the deformation bands. However, if the fluid flow is horizontal to the deformation bands, the bands tend to act as partial barriers. In this study, the bands with N-S and NE-SW orientations caused a barrier effect to the fluid flow in the vertical direction. On the other hand, the vertical (NE-SW) and sub-vertical (E-W) bands showed resistance to flow in the horizontal direction. In this context, we interpret that the X - node is characterized by the intersection of the N-S and NE-SW bands, while the Y - node is characterized by the interaction between the deformation bands with E-W and NE-SW orientation. According to simulation results by Souza et al. (2022), we suggest that in vertical flow (Kvert) the resistance to fluid flow will be greater when the fluid crosses the X- nodes, and secondarily the Y - nodes. In contrast, in horizontal flow (Khor) the difficulty of fluid migration in a connection will be greater in the damage zone at X - nodes, followed by Y – node (Figure 4.15). Our results showed that permeability is lower at X - node in

both planes, with difficult to fluid migration in this type of connection. I - Node has higher permeability values and predominates within the fault core and damage zone in the XY plane, showing a preference for fluid flow in this type of connection. On the other hand, the Y-node presents greater permeability in the core in the XY plane, whose architectural element has deformation bands with an anastomosed pattern. In this case, the fluid flow resistance will be lower in the vertical flow (Kvert), as the flow direction is parallel to the structures (Figure 4.15). Therefore, the distribution of connections along a fault zone is relevant to understanding connections' influence on fluid flow in a reservoir affected by deformation bands. Thus, the type of nodes impacts the fluid flow a priori in X-nodes, while the fluid obstacle is smaller in Y-nodes and nodes-I.

Finally, Stohler et al. (2022) evaluated the impact of deformation bands on fault zone architectural elements with 3D modeling and numeric simulation. These authors considered in workflow, the equivalent permeability in the damage zone and transmissibility multipliers fault in the fault core. In this work, it was demonstrated that deformation bands in damage zones and fault core reduce the performance of hydrocarbon reservoir, presenting lower production and higher injection pressure. From the above, we interpret that both the damage zone and the fault core of the studied area can impact the fluid flow.

4.6. Conclusions

Our study presents new data for topological analysis in three dimensions with deformation bands integrated with structural and petrophysical characterization. Our results indicate the following conclusions:

- 1) The connectivity pattern varies across the fault zone. In the fault core, Y-nodes are dominant, followed by X- and I -nodes. The damage zone is dominated by Y-nodes, and secondarily I- and X-nodes.
- 2) Furthermore, the deformation band network has domain of completely connected branches (C-C) in the damage zone and core in both planes. In contrast, partially connected branches (I-C) do not occur in the core in the XZ plane.
- 3) The fault zone analyzed presents new nodes. The nodes were defined as H and W presenting five and six branches, respectively. The H- and W-nodes are

formed when a syn-rift fault system crosscut with a post-rift fault system. The difference between them consists on the vertical fault. If this fault crosses the intersection point of the antithetic and synthetic faults, the W-node is formed. On the other hand, if the vertical fault does not cross the intersection of the synthetic and antithetic faults, the H-node is formed.

- 4) The permeability is anisotropic along the fault zone. The permeability in the architectural elements of the fault zone (core and damage zone) varies according to the type of connection, with higher values in the core for I-node, secondarily for Y-node, and lower for X-node. In the damage zone, the XZ plane has higher permeabilities at the I-node, followed by the Y- and X-nodes. However, the XY plane follows the sequence of higher permeabilities for the I-, X-, and Y-nodes. Therefore, a greater connection tends to reduce the permeability. Nevertheless, the anisotropy also influences the permeability: $K_{horizontal} < K_{vertical}$.
- 5) In (Khor) horizontal flow, fault core connections tend to act as a barrier. On the other hand, in vertical flow (K_{vert}), the connections of the core and the damage zone can act as barriers.
- 6) This study approach, which uses the deformation band topology applied to the permeability characterization, may contribute to modeling and simulating reservoirs aiming at the impact of the connectivity variation in the fluid flow. Thus, we suggest that future research consider topological parameters in their modeling and that such parameters be tested in fluid flow numerical simulations.
- 7) The topological analysis of the vertical exposure deformation bands (XZ plane) showed limitation due to the deformation intensity. In future works, we suggest analyzing the cataclasis intensity (protocataclasites and ultracataclasites).

References

Antonellini, M.A., Aydin, A., Pollard, D.D., 1994. **Microstructure of deformation bands in porous sandstones at Arches National Park, Utah**. Journal of Structural Geology 16, 941–959. [https://doi.org/10.1016/0191-8141\(94\)90077-9](https://doi.org/10.1016/0191-8141(94)90077-9).

Arai, M., 2006. **Revisão Estratigráfica do Cretáceo Inferior das Bacias Interiores do Nordeste do Brasil**. Petróleo Brasileiro S.A. São Paulo, UNESP, Geociências 25, 1, 7-15.

Araujo, R.E.B., Bezerra, F.H.R., Nogueira, F.C.C., Balsamo, F., Carvalho, B.R.B.M., Souza, J.A.B., Sanglard, J.C.D., de Castro, D.L., Melo, A.C.C., 2018. **Basement control on fault formation and deformation band damage zone evolution in the Rio do Peixe Basin, Brazil**. Tectonophysics 745, 117–131. <https://doi.org/10.1016/j.tecto.2018.08.011>.

Aydin, A., Johnson, A.M., 1978. **Development of faults as zones of deformation bands and as slip surfaces in sandstone**. Pure and Applied Geophysics 116 (4-5), 931-942. <https://doi.org/10.1007/BF00876547>.

Awdal, A., Surmairy, R., Singh, K., Fabre, G., Alsop, G.I., 2020. **Deformation bands and their impact on fluid flow: insights from geometrical modeling and multi-scale flow simulations in sandstones**. Journal of Structural Geology 141, 104215. <https://doi.org/10.1016/j.jsg.2020.104215>.

Ballas, G., Fossen, H., Soliva, R., 2015. **Factors controlling the permeability of cataclastic deformation bands and faults in porous sandstone reservoirs**. Journal of Structural Geology. 76, 1–21. <https://doi.org/10.1016/j.jsg.2015.03.013>.

Ballas, G., Soliva, R., Benedicto, A., Sizun, J.P., 2014. **Control of tectonic setting and large-scale faults on the basin-scale distribution of deformation bands in porous sandstone (Provence, France)**. Marine and Petroleum Geology 55, 142–159. <https://doi.org/10.1016/j.marpetgeo.2013.12.020>.

Balsamo, F., Storti, F., Salvini, F., Silva, A.T., Lima, C.C., 2010. **Structural and petrophysical evolution of extensional fault zones in low-porosity, poorly lithified sandstones of the Barreiras Formation, NE Brazil**. Journal of Structural Geology 32, 1806–1826. <https://doi.org/10.1016/j.jsg.2009.10.010>.

Berkowitz, B., 1995. **Analysis of fracture network connectivity using percolation theory**. Mathematical Geology 27, 467–483. <https://doi.org/10.1007/BF02084422>.

Bonato, J., Tognoli, F.M.W., Nogueira, F.C.C., Miranda, T.S., Inocencio, L.C., 2022. **The use of network topology to assess connectivity of deformation bands in sandstone: A quantitative approach based on digital outcrop models.** *Journal of Structural Geology* 161, 104682. <https://doi.org/10.1016/j.jsg.2022.104682>.

Braathen, A., Tveranger, J., Fossen, H., Skar, T., Cardozo, N., Semshaug, S.E., Bastesen, E., Sverdrup, E., 2009. **Fault facies and their application to sandstone reservoirs.** *American Association of Petroleum Geologists* 93, 891–917. <http://dx.doi.org/10.1306/03230908116>.

Caine, J.S., Evans, J.P., Forster, C.B., 1996. **Fault zone architecture and permeability structure.** *Geology* 24, 1025–1028. [https://doi.org/10.1130/0091-7613\(1996\)024<1025:FZAAPS>2.3.CO;2](https://doi.org/10.1130/0091-7613(1996)024<1025:FZAAPS>2.3.CO;2).

Childs, C., Manzocchi, T., Walsh, J.J., Bonson, C.G., Nicol, A., Schöpfer, M.P.J., 2009. **A geometric model of the fault zone and fault rock thickness variations.** *Journal of Structural Geology* 31, 117–127. <https://doi.org/10.1016/j.jsg.2008.08.009>.

De Castro, D.L., Oliveira, D.C., Castelo Branco, R.M.G., 2007. **On the tectonics of the Neocomian Rio do Peixe Rift Basin, NE Brazil: Lessons from gravity, magnetic and radiometric data.** *Journal of South American Earth Sciences* 24, 184–202. <https://doi.org/10.1016/j.jsames.2007.04.001>.

De Souza, D.H.S., Nogueira, F.C.C., Vasconcelos, D.L., Torabi, A., Souza, J.A.B., Nicchio, M., Perez, Y.A.R., Balsamo, F., 2021. **Growth of cataclastic bands into a fault zone: A multiscale process by microcrack coalescence in sandstones of Rio do Peixe Basin, NE Brazil.** *Journal of Structural Geology* 146, 104315. <https://doi.org/10.1016/j.jsg.2021.104315>.

Dershowitz, W.S.; Herda, H.H., 1992. **Interpretation of fracture spacing and intensity.** *Proceedings of the 33rd US Symposium on Rock Mechanics.* Santa Fé, 1992, 757–766.

Françolin, J.B.L., Cobbold, P.R., Szatmari, P., 1994. **Faulting in the Early Cretaceous Rio do Peixe basin (NE Brazil) and its significance for the opening**

of the Atlantic. Journal of Structural Geology 16, 647–661.
[https://doi.org/10.1016/0191-8141\(94\)90116-3](https://doi.org/10.1016/0191-8141(94)90116-3).

Fossen, H., Bale, A., 2007. **Deformation bands and their influence on fluid flow.** American Association of Petroleum Geologists 91, 1685–1700.
<https://doi.org/10.1306/07300706146>.

Fossen, H., Johansen, T.E.S., Hesthammer, J., Rotevatn, A. 2005. **Fault interaction in porous sandstone and implications for reservoir management; examples from southern Utah.** American Association of Petroleum Geologists 89, 1593–1606.
<https://doi.org/10.1306/07290505041>.

Fossen, H., Soliva, R., Ballas, G., Trzaskos, B., Cavalcante, C., Schultz, R.A., 2017. **A Review of Deformation Bands in Reservoir Sandstones: Geometries, Mechanisms and Distribution.** Geological Society of London, Special Publications 459, 9–33. <https://doi.org/10.1144/SP459.4>

Gjesteland, B.M.V., 2020. **Geometry and topology of deformation band networks in wall damage zones and intersection damage zones.** Master Thesis. University Of Bergen, Department of Earth Science, 91.

Jing, L., Stephansson, O., 1997. **Network topology and homogenization of fractured rocks.** In: Jamtveit, B., Yardley, B.W. (Eds.), Fluid Flow and Transport in Rocks. Mechanisms and Effects. Chapman & Hall, Oxford, 191–202.

Manzocchi, T., 2002. **The connectivity of two-dimensional networks of spatially correlated fractures.** Water Resources Research 38, 1–20.
<http://dx.doi.org/10.1029/2000WR000180>.

Micarelli, L., Moretti, I., Daniel, J.M., 2003. **Structural properties of rift-related normal faults: the case study of the Gulf of Corinth, Greece.** Journal of Geodynamics 36, 275–303. [https://doi.org/10.1016/S0264-3707\(03\)00051-6](https://doi.org/10.1016/S0264-3707(03)00051-6).

Morley, C.K., Nixon, C.W. 2016. **Topological characteristics of simple and complex normal fault networks.** Journal of Structural Geology 84, 68-84.
<https://doi.org/10.1016/j.jsg.2016.01.005>.

Nicchio, M.A., Nogueira, F.C.C., Balsamo, F., Souza, J.A.B., Carvalho, B.R.B.M., Bezerra, F.H.R., 2018. **Development of cataclastic foliation in deformation bands in feldspar-rich conglomerates of the Rio do Peixe Basin, NE Brazil.** *Journal of Structural Geology* 107, 132–141. <https://doi.org/10.1016/j.jsg.2017.12.013>.

Nicchio, M.A., Balsamo, F., Cifelli, F., Nogueira, F.C.C., Aldega, L., Bezerra, F.H.R., 2022a. **An integrated structural and magnetic fabric study to constrain the progressive extensional tectonics of the Rio do Peixe Basin, Brazil.** *Tectonics* 41, e2022TC007244. <https://doi.org/10.1029/2022TC007244>.

Nicchio, M.A., Balsamo, F., Nogueira, F.C.C., Aldega, L., Pontes, C.C.C., Bezerra, F.H., Souza, J.A.B., 2022b. **The effect of fault-induced compaction on petrophysical properties of deformation bands in poorly lithified sandstones.** *Journal of Structural Geology* 166, 104758. <https://doi.org/10.1016/j.jsg.2022.104758>.

Nogueira, F.C.C., Marques, F.O., Bezerra, F.H.R., de Castro, D.L., Fuck, R.A., 2015. **Cretaceous intracontinental rifting and post-rift inversion in NE Brazil: Insights from the Rio do Peixe Basin.** *Tectonophysics* 644–645, 92–107. <https://doi.org/10.1016/j.tecto.2014.12.016>

Nogueira, F.C.C., Nicchio, M.A., Balsamo, F., Souza, J.A.B., Silva, I.V.L., Bezerra, F.H.R., Vasconcelos, D.L., Carvalho, B.R.B.M., 2021. **The influence of the cataclastic matrix on the petrophysical properties of deformation bands in arkosic sandstones.** *Marine and Petroleum Geology* 124, 104825. <https://doi.org/10.1016/j.marpetgeo.2020.104825>.

Nyberg, B., Nixon, C.W., Sanderson, D.J., 2018. **NetworkGT: a GIS tool for geometric and topological analysis of two-dimensional fracture networks.** *Geosphere* 14, 1618–1634. <https://doi.org/10.1130/GES01595.1>.

Oliveira, L.S.B., Nogueira, F.C.C., Vasconcelos, D.L., Balsamo, F., Bezerra, F.H.R., Pérez, Y.A.R., 2022. **Mechanical stratigraphy influences deformation band pattern in arkosic sandstones, Rio do Peixe Basin, Brazil.** *Journal of Structural Geology* 155, 104510. <https://doi.org/10.1016/j.jsg.2022.104510>.

Palhano, L.C, Nogueira, F.C.C, Marques, F.O, Vasconcelos, D.L., Bezerra, F.H., Souza, J.A.B., Nicchio, M.A., Perez, Y.A.R., Balsamo, F., 2023. **Influence of hydrothermal silicification on the physical properties of a basin-boundary fault affecting arkosic porous sandstones, Rio do Peixe Basin, Brazil.** Marine and Petroleum Geology 148, 106062. <https://doi.org/10.1016/j.marpetgeo.2022.106062>.

Parnell, J., Watt, G.R., Middleton, D., Kelly, J., Baron, M., 2004. **Deformation band control on hydrocarbon migration.** Journal of Sedimentary Research 74, 552–560. <https://doi.org/10.1306/121703740552>.

Pontes, C.C.C., Nogueira, F.C.C., Bezerra, F.H.R., Balsamo, F., Miranda, T.S., Nicchio, M. A., Souza, J.A.B., Carvalho, B.R.B.M., 2019. **Petrophysical properties of deformation bands in high porous sandstones across fault zones in the Rio do Peixe Basin, Brazil.** International Journal of Rock Mechanics and Mining Sciences. 114, 153–163. <https://doi.org/10.1016/j.ijrmms.2018.12.009>.

Ramos, G.V., Vasconcelos, D.L., Marques, F.O., de Castro, D.L., Nogueira, F.C.C., Bezerra, F.H.R., Perez, Y.A.R., Souza, J.A.B., Medeiros, V.C., 2022. **Relations between inherited basement fabric and fault nucleation in a continental setting: The Rio do Peixe Basin, NE Brazil.** Marine and Petroleum Geology 139, 105635. <https://doi.org/10.1016/j.marpetgeo.2022.105635>.

Roesner, H.E., Lana, C.C., Le Herissé, A., Melo, J.H.G., 2011. **Bacia do Rio do Peixe (PB). Novos resultados biocronoestratigráficos e paleoambientais.** In: Carvalho, I.S., Srivastava, N.K., Strohschoen, Jr, O., Lana C.C., (Eds.), Paleontologia: Cenários de Vida, 3. Rio de Janeiro. Interciência 135–141.

Romano, C.R., Garing, C., Minto, J.M., Benson, S.M., Shipton, Z.K., Lunn, R.J., 2020. **Extreme capillary heterogeneities and in situ fluid compartmentalization due to clusters of deformation bands in sandstones.** International Journal of Greenhouse Gas Control 106, 103280. <https://doi.org/10.1016/j.ijggc.2021.103280>.

Rotevatn, A., Sandve, T., Keilegavlen, E., Kolyukhin, D., Fossen, H. 2013. **Deformation bands and their impact on fluid flow in sandstone reservoirs: the**

role of natural thickness variations. *Geofluids* 13, 359–371.
<https://doi.org/10.1111/gfl.12030>.

Rotevatn, A., Tveranger, J., Howell, J., Fossen, H. 2009. **Dynamic investigation of the effect of a relay ramp on simulated fluid flow: geocellular modeling of the Delicate Arch Ramp, Utah.** *Petroleum Geoscience* 15, 45–58.
<https://doi.org/10.1144/1354-079309-77>.

Rotevatn, A., Fossen, H., Hesthammer, J., Howell, J.A., 2007. **Are relay ramps conduits for fluid flow? Structural analysis of a relay ramp in Arches National Park, Utah.** In: Lonergan, L., Jolly, R.J.H., Sanderson, D.J., Rawnsley, K. (Eds.), *Fractured Reservoirs*. Geological Society, London, Special Publications 270, 55–71.
<https://doi.org/10.1144/GSL.SP.2007.270.01.04>.

Saevik, P.N., Nixon, C.W., 2017. **Inclusion of topological measurements into analytic estimates of effective permeability in fractured media.** *Water Resources Research* 53, 9424–9443. <https://doi.org/10.1002/2017WR020943>.

Sanderson, D.J., Nixon, C.W., 2015. **The use of topology in fracture network characterization.** *Journal of Structural Geology* 72, 55–66.
<https://doi.org/10.1016/j.jsg.2015.01.005>

Sénant, J., Popoff, M., 1991. **Early Cretaceous extension in northeast Brazil related to the South Atlantic opening.** *Tectonophysics* 198, 35–46.
[https://doi.org/10.1016/0040-1951\(91\)90129-G](https://doi.org/10.1016/0040-1951(91)90129-G).

Silva, M.E., Nogueira, F.C.C., Pérez, Y.A.R., Vasconcelos, D.L., Stohler, R.C., Sanglard, J.C.D., Balsamo, F., Bezerra, F.H.R., Carvalho, B.R.B.M., Souza, J.A.B., 2022. **Permeability modeling of a basin-bounding fault damage zone in the Rio do Peixe Basin, Brazil.** *Marine and Petroleum Geology* 135, 105409.
<https://doi.org/10.1016/j.marpetgeo.2021.105409>.

Souza, F.M., Gomes, I.F., Nogueira, F.C.C., Vasconcelos, D.L., Canabarro, B., Souza, J.A.B., Guimarães, L.J.N., Beserra, L.B.S., 2022. **2D modeling and simulation of deformation bands' effect on fluid flow: Implications for hydraulic properties in**

siliciclastic reservoirs. Journal of Structural Geology 158, 104581. <https://doi.org/10.1016/j.jsg.2022.104581>.

Stohler, R. C; Nogueira, F.C.C; Mello, C.L; Souza, J.A.B., 2022. **3D numerical modeling and simulation of the impact of fault zones on fluid flow in sandstones of the Rio do Peixe Basin, NE Brazil.** Petroleum Geoscience 28 (4). <https://doi.org/10.1144/petgeo2022-024>

Torabi, A., Balsamo, F., Nogueira, F.C.C., Vasconcelos, D.L., Silva, A.C.E., Bezerra, F.H. R., Souza, J.A.B., 2021. **Variation of thickness, internal structure and petrophysical properties in a deformation band fault zone in siliciclastic rocks.** Marine and Petroleum Geology 133, 105297. <https://doi.org/10.1016/j.marpetgeo.2021.105297>.

Torabi, A., Fossen, H., 2009. **Spatial variation of microstructure and petrophysical properties along deformation bands in reservoir sandstones.** American Association of Petroleum Geologists 93, 919–938. <https://doi.org/10.1306/03270908161>.

Vagle, E.B., 2020. **Topology and distribution of deformation bands in normal fault damage zones, Utah.** Master Thesis. University of Bergen, Department of Earth Science, 117.

Vasconcelos, D.L., Marques, F.O., Nogueira, F.C.C., Perez, Y.A.R., Bezerra, F.H.R., Stohler, R.C., Souza, J.A.B., 2021. **Tectonic inversion is assessed by the integration of geological and geophysical data: The intracontinental Rio do Peixe Basin, NE Brazil.** Basin Research 33, 705–728. <https://doi.org/10.1111/bre.12491>.

Wibberley, C.A.J., Pettit, J.P., Rives, T., 2007. **The mechanics of fault distribution and localization in high-porosity sands, Provence, France.** Geological Society of London, Special Publications 289, 19–46. <https://doi.org/10.1144/SP289.3>.

Wilson, P.I.R., Wilson, R.W., Sanderson, D.J., Jarvis, I., McCaffrey, K.J.W., 2021. **Analysis of deformation bands associated with the Trachyte Mesa intrusion, Henry Mountains, Utah: implications for reservoir connectivity and fluid flow**

around sill intrusions. Solid Earth 12, 95–117. <https://doi.org/10.5194/se-12-95-2021>.

Zuluaga, L.F., Rotevatn, A., Keilegavlen, E., Fossen, H., 2016. **The impact of deformation bands on simulated fluid flow within fault-propagation fold trap types: lessons from the San Rafael Monocline, Utah (USA).** American Association of Petroleum Geologists 100, 1523–1540. <https://doi.org/10.1306/04151614153>.

Capítulo 5

Conclusões e sugestões para trabalhos futuros

5. Conclusões e sugestões para trabalhos futuros

O presente trabalho mostrou relevância no entendimento da influência das conexões de bandas de deformação na propriedade de fluxo de fluido nos elementos arquiteturais (núcleo e zona de dano) de uma zona de falha da Bacia Rio do Peixe, com exposição tridimensional (vertical e horizontal). Nesse contexto, é possível realizar algumas conclusões acerca dos resultados obtidos:

- Os elementos arquiteturais da zona de falha possuem espessura média de: 1 metro no núcleo, 1 metro no hanging wall e 7 metros no footwall.
- A porção do afloramento estudado possui dois sistemas de falhas que se cruzam: um sin-rifte e um pós-rifte. Esses sistemas determinam a formação dos nós H e W, formados por cinco e seis ramos que interceptam o mesmo ponto.
- Em ambos os planos, as estruturas possuem padrão anastomosado no núcleo de falha e padrão romboédrico na zona de dano.
- O padrão de conectividade varia ao longo da zona de falha. O núcleo de falha tem pedomínio de nós Y, seguido de nós X e nós I. A zona de dano possui domínio de nós Y, e secundariamente nós I e nós X.
- Além disso, a rede de bandas de deformação possui domínio de ramos completamente conectados (C-C) na zona de dano e núcleo em ambos os planos. Em contraste, ramos parcialmente conectados (I-C) não ocorrem no núcleo no plano XZ.
- A permeabilidade é anisotrópica ao longo da zona de falha. O impacto das conexões na permeabilidade é maior nos nós X, seguido dos nós Y e I, para o núcleo de falha em ambos os planos. Em contraste, a permeabilidade será menor na zona de dano no plano XZ nos nós X, seguido dos nós Y e nós I. No plano XY, a permeabilidade é menor nos nós Y, e secundariamente nos nós X e I.
- No fluxo horizontal (K_y), as conexões do núcleo da falha tendem a atuar como uma barreira. Por outro lado, no fluxo vertical (K_z), as conexões do núcleo e da zona de dano podem atuar como barreiras.

Em trabalhos subsequentes, sugerimos a realização de análise de cataclase no núcleo de falha, afim de avaliar a intensidade de deformação nesse elemento arquitetural e seu efeito na aquisição de permeabilidade e análise topológica. Outra

sugestão para trabalhos futuros é considerar os parâmetros topológicos em modelagem e que tais parâmetros sejam testados em simulações numéricas de fluxo de fluidos.

Referências

Antonellini, M.A., Aydin, A., Pollard, D.D., 1994. **Microstructure of deformation bands in porous sandstones at Arches National Park, Utah**. *Journal of Structural Geology* 16, 941–959. [https://doi.org/10.1016/0191-8141\(94\)90077-9](https://doi.org/10.1016/0191-8141(94)90077-9).

Araujo, R.E.B., Bezerra, F.H.R., Nogueira, F.C.C., Balsamo, F., Carvalho, B.R.B.M., Souza, J.A.B., Sanglard, J.C.D., de Castro, D.L., Melo, A.C.C., 2018. **Basement control on fault formation and deformation band damage zone evolution in the Rio do Peixe Basin, Brazil**. *Tectonophysics* 745, 117–131. <https://doi.org/10.1016/j.tecto.2018.08.011>.

Aydin, A.; Johnson, A. M. 1978. **Development of faults as zones of deformation bands and as slip surfaces in sandstone**. *Pure and applied Geophysics* 116 (4-5), 931-942. <https://doi.org/10.1007/BF00876547>.

Awdal, A., Surmairy, R., Singh, K., Fabre, G., Alsop, G.I., 2020. **Deformation bands and their impact on fluid flow: insights from geometrical modelling and multi-scale flow simulations in sandstones**. *Journal of Structural Geology* 141, 104215 <https://doi.org/10.1016/j.jsg.2020.104215>.

Ballas, G., Fossen, H., Soliva, R., 2015. **Factors controlling permeability of cataclastic deformation bands and faults in porous sandstone reservoirs**. *Journal of Structural Geology* 76, 1–21. <http://dx.doi.org/10.1016/j.jsg.2015.03.013>.

Ballas, G., Soliva, R., Benedicto, A., Sizun, J.P., 2014. **Control of tectonic setting and large-scale faults on the basin-scale distribution of deformation bands in porous sandstone (Provence, France)**. *Marine and Petroleum Geology* 55, 142–159. <https://doi.org/10.1016/j.marpetgeo.2013.12.020>.

Balsamo, F., Storti, F., Salvini, F., Silva, A.T., Lima, C.C., 2010. **Structural and petrophysical evolution of extensional fault zones in low-porosity, poorly**

lithified sandstones of the Barreiras Formation, NE Brazil. *Journal of Structural Geology* 32, 1806–1826. <https://doi.org/10.1016/j.jsg.2009.10.010>.

Berg, S.S., Skar, T., 2005. **Controls on damage zone asymmetry of a normal fault zone: outcrop analyses of a segment of the Moab fault, SE Utah.** *Journal of Structural Geology* 27, 1803–1822. <http://dx.doi.org/10.1016/j.jsg.2005.04.012>.

Boccaletti, S., Latora, V., Moreno, Y., Chavez, M., Hwang, D.U., 2006. **Complex networks: Structure and dynamics.** *Physics reports* 424(4-5), 175-308. <https://doi.org/10.1016/j.physrep.2005.10.009>.

Bonato, J., Tognoli, F.M.W., Nogueira, F.C.C., Miranda, T.S., Inocencio, L.C., 2022. **The use of network topology to assess connectivity of deformation bands in sandstone: A quantitative approach based on digital outcrop models.** *Journal of Structural Geology* 161. <https://doi.org/10.1016/j.jsg.2022.104682>.

Braathen, A., Tveranger, J., Fossen, H., Skar, T., Cardozo, N., Semshaug, S.E., Bastesen, E., Sverdrup, E., 2009. **Fault facies and its application to sandstone reservoirs.** *American Association of Petroleum Geologists* 93, 891–917. <http://dx.doi.org/10.1306/03230908116>.

Braun, O.P.G., 1969. *Geologia da Bacia do Rio do Peixe, Nordeste do Brasil. Relatório de Prospeção., Ministério de Minas e Energia.* Departamento Nacional de Produção Mineral (DNPM), Natal 4º Distrito do Nordeste.

Caine, J.S., Evans, J.P., Forster, C.B., 1996. **Fault zone architecture and permeability structure.** *Geology* 24, 1025–1028. [https://doi.org/10.1130/0091-7613\(1996\)024<1025:FZAAPS>2.3.CO;2](https://doi.org/10.1130/0091-7613(1996)024<1025:FZAAPS>2.3.CO;2).

Carvalho, I. S., Mendes, J. C., Costa, T., 2013. **The role of fracturing and mineralogical alteration of basement gneiss in the oil exudation in the Sousa Basin (Lower Cretaceous), Northeastern Brazil.** *Journal of South American Earth Sciences* 47, 47–54. <https://doi.org/10.1016/j.jsames.2013.06.001>.

Childs, C., Manzocchi, T., Walsh, J.J., Bonson, C.G., Nicol, A., Schöpfer, M.P.J., 2009. **A geometric model of fault zone and fault rock thickness variations.** *Journal of Structural Geology* 31, 117–127. <https://doi.org/10.1016/j.jsg.2008.08.009>.

Choi, J.H., Edwards, P., Ko, K., Kim, Y.S., 2016. **Definition and classification of fault damage zones: A review and a new methodological approach.** *Earth-Science Reviews* 152, 70–87. <http://dx.doi.org/10.1016/j.earscirev.2015.11.006>.

Carvalho, I.S., 2020. **Geological environments of dinosaur footprints in the intracratonic basins of northeast Brazil during the Early Cretaceous opening of the South Atlantic.** *Cretaceous Research* (2000) 21, 255–267. <https://doi.org/10.1006/cres.1999.0194>.

de Castro, D.L., Oliveira, D.C., Castelo Branco, R.M.G., 2007. **On the tectonics of the Neocomian Rio do Peixe Rifting Basin, NE Brazil: Lessons from gravity, magnetic and radiometric data.** *Journal of South American Earth Sciences* 24, 184–202. <https://doi.org/10.1016/j.jsames.2007.04.001>.

Dershowitz, W.S., Einstein, H.H., 1988. **Characterizing rock joint geometry with joint system models.** *Rock Mechanics and Rock Engineering* 21, 21–51. <https://doi.org/10.1007/BF01019674>.

Dershowitz, W.S., Herda, H.H., 1992. **Interpretation of fracture spacing and intensity. Proceedings of the 33rd US Symposium on Rock Mechanics.** Santa Fé, 1992, 757 – 766.

de Souza, D.H.S., Nogueira, F.C.C., Vasconcelos, D.L., Torabi, A., de Souza, J.A.B.; Nicchio, M.A., Pérez, Y.A.R., Balsamo, F., 2021. **Growth of cataclastic bands into a fault zone: a multiscalar process by microcrack coalescence in sandstones of Rio do Peixe Basin, NE Brazil.** *Journal of Structural Geology* 146 <https://doi.org/10.1016/j.jsg.2021.104315>.

Faulkner, D.R., Jackson, C.A.L., Lunn, R.J., Schlische, R.W., Shipton, Z.K., Wibberley, C.A.J., Withjack, M.O., 2010. **A review of recent developments concerning the structure, mechanics and fluid flow properties of fault zones.** *Journal of Structural Geology* 32, 1557- 1575. <https://doi.org/10.1016/j.jsg.2010.06.009>.

Fossen, H., Bale, A., 2007. **Deformation bands and their influence on fluid flow.** *AAPG (American Association of Petroleum Geologists)* 91, 1685–1700. <https://doi.org/10.1306/07300706146>.

Fossen, H., Soliva, R., Ballas, G., Trzaskos, B., Cavalcante, C., Schultz, R.A., 2017. **A Review of Deformation Bands in Reservoir Sandstones: Geometries, Mechanisms and Distribution**. Geological Society, London. Special Publications SP459.4. <https://doi.org/10.1144/SP459.4>.

Françolin, J.B.L., Cobbold, P.R.M., Szatmari, P., 1994. **Faulting in the Early Cretaceous Rio do Peixe (NE Brazil) and its significance for the opening of the Atlantic**. Journal of Structural Geology 16, 647–661. [https://doi.org/10.1016/0191-8141\(94\)90116-3](https://doi.org/10.1016/0191-8141(94)90116-3)

Gjesteland, B.M.V., 2020. **Geometry and topology of deformation band networks in wall damage zones and intersection damage zones**. Master Thesis. University Of Bergen, Department of Earth Science. 91.

Ma, D.B., Wu, G.H., Scarselli, N., Luo, X.S., Han, J.F., Chen, Z.Y., 2019. **Seismic damage zone and width-throw scaling along the strike-slip faults in the Ordovician carbonates in the Tarim Basin**. Petroleum Science 16, 752–762. <https://doi.org/10.1007/s12182-019-0352-4>.

Manzocchi, T., 2002. **The connectivity of two dimensional networks of spatially correlated fractures**. Water Resources Research 38, 9, 1162. <http://dx.doi.org/10.1029/2000WR000180>.

Marques, F.O., Nogueira, F.C.C., Bezerra, F.H.R., de Castro, D.L., 2014. **The Araripe Basin in NE Brazil: An intracontinental graben inverted to a high-standing horst**. Tectonophysics 630, 251–264. <https://doi.org/10.1016/j.tecto.2014.05.029>.

Medeiros, W.E., do Nascimento, A.F., Alves da Silva, F.C., Destro, N., Demétrio, J.G.A., 2010. **Evidence of hydraulic connectivity across deformation bands from field pumping tests: Two examples from Tucano Basin, NE Brazil**. Journal of Structural Geology 32, 1783–1791. <https://doi.org/10.1016/j.jsg.2009.08.019>.

Micarelli, L., Moretti, I., Daniel, J.M., 2003. **Structural properties of rift-related normal faults: the case study of the Gulf of Corinth, Greece**. Journal of Geodynamics 36, 275–303. [https://doi.org/10.1016/S0264-3707\(03\)00051-6](https://doi.org/10.1016/S0264-3707(03)00051-6).

Morley, C.K., Nixon, C.W. 2016. **Topological characteristics of simple and complex normal fault networks**. *Journal of Structural Geology* 84, 68-84. <https://doi.org/10.1016/j.jsg.2016.01.005>.

Nicchio, M.A., Balsamo, F., Cifelli, F., Nogueira, F.C.C., Aldega, L., Bezerra, F.H.R., 2022(a). **An integrated structural and magnetic fabric study to constrain the progressive extensional tectonics of the Rio do Peixe Basin, Brazil**. *Tectonics* 41. doi:10.1029/2022TC007244.

Nicchio, M.A., Nogueira, F.C.C., Balsamo, F., Souza, J.A.B., Carvalho, B.R.B.M, Bezerra, F.H.R., 2018. **Development of cataclastic foliation in deformation bands in feldspar-rich conglomerates of the Rio do Peixe Basin, NE Brazil**. *Journal of Structural Geology* 107, 132–141. <https://doi.org/10.1016/j.jsg.2017.12.013>

Nixon, C. W.; Kari Naerland, K.; Rotevatn, A.; Vilde Dimmen, V.; Sanderson, D. J.; Kristensen, T. B., 2020. **Connectivity and network development of carbonate-hosted fault damage zones from western Malta**. *Journal of Structural Geology* 141, 104212. <https://doi.org/10.1016/j.jsg.2020.104212>

Nogueira, F.C.C., Marques, F.O., Bezerra, F.H.R., de Castro, D.L., Fuck, R.A., 2015. **Cretaceous intracontinental rifting and post-rifte inversion in NE Brazil: Insights from the Rio do Peixe Basin**. *Tectonophysics* 644–645, 92–107. <https://doi.org/10.1016/j.tecto.2014.12.016>

Nogueira, F.C.C., Nicchio, M.A., Balsamo, F., Souza, J.A.B., Silva, I.V.L., Bezerra, F.H.R., Vasconcelos, D.L., Carvalho, B.R.B.M., 2021. **The influence of the cataclastic matrix on the petrophysical properties of deformation bands in arkosic sandstones**. *Marine and Petroleum Geology* 124, 104825. <https://doi.org/10.1016/j.marpetgeo.2020.104825>.

Nyberg, B., Nixon, C.W., Sanderson, D.J., 2018. **NetworkGT: a GIS tool for geometric and topological analysis of two-dimensional fracture networks**. *Geosphere* 14, 1618–1634. <https://doi.org/10.1130/GES01595.1>.

Oliveira, L.S.B., Nogueira, F.C.C., Vasconcelos, D.L., Balsamo, F., Bezerra, F.H.R., Pérez, Y.A.R., 2022. **Mechanical stratigraphy influences deformation band**

pattern in arkosic sandstones, Rio do Peixe Basin, Brazil. *Journal of Structural Geology* 155, 104510 <https://doi.org/10.1016/j.jsg.2022.104510>.

Palhano, L.C, Nogueira, F.C.C, Marques, F.O, Vasconcelos, D.L., Bezerra, F.H., Souza, J.A.B., Nicchio, M.A., Perez, Y.A.R., Balsamo, F., 2023. **Influence of hydrothermal silicification on the physical properties of a basin-boundary fault affecting arkosic porous sandstones, Rio do Peixe Basin, Brazil.** *Marine and Petroleum Geology* 148, 106062. <https://doi.org/10.1016/j.marpetgeo.2022.106062>.

Parnell, J., Watt, G. R., Middleton, D., Kelly, J., Baron, M., 2004. **Deformation band control on hydrocarbon migration.** *Journal of Sedimentary Research* 74(4), 552-560. <https://doi.org/10.1306/121703740552>.

Pontes, C.C.C., Nogueira, F.C.C., Bezerra, F.H.R., Balsamo, F., Miranda, T.S., Nicchio, M. A., Souza, J.A.B., Carvalho, B.R.B.M., 2019. **Petrophysical properties of deformation bands in high porous sandstones across fault zones in the Rio do Peixe Basin, Brazil.** *Journal of Rock Mechanics* 114, 153–163. <https://doi.org/10.1016/j.ijrmms.2018.12.009>.

Ramos, G.V., Vasconcelos, D.L., Marques, F.O., de Castro, D.L., Nogueira, F.C.C., Bezerra, F.H.R., Perez, Y.A.R., Souza, J.A.B., Medeiros, V.C., 2022. **Relations between inherited basement fabric and fault nucleation in a continental setting: The Rio do Peixe Basin, NE Brazil.** *Marine and Petroleum Geology* 139. <https://doi.org/10.1016/j.marpetgeo.2022.105635>.

Roesner, H.E., Lana, C.C., Le Herissé, A., Melo, J.H.G., 2011. Bacia do Rio do Peixe 820 (PB). **Novos resultados biocronoestratigráficos e paleoambientais.** In: Carvalho, I.S., 821 Srivastava, N.K., Strohschoen, Jr, O., Lana C.C., (Eds.), *Paleontologia: Cenários de 822 Vida*, 3. Rio de Janeiro. *Interciência* 135–141.

Romano, C.R., Garing, C., Minto, J.M., Benson, S.M., Shipton, Z.K., Lunn, R.J., 2020. **Extreme capillary heterogeneities and in situ fluid compartmentalization due to clusters of deformation bands in sandstones.** *International Journal of Greenhouse Gas Control* 106, 103280. <https://doi.org/10.1016/j.ijggc.2021.103280>.

Rotevatn, A., Fossen, H., Hesthammer, J., Aas, T.E., Howell, J.A., 2007. **Are relay ramps conduits for fluid flow? Structural analysis of a relay ramp in Arches**

National Park, Utah. In: Lonergan, L., Jolly, R.J.H., Sanderson, D.J., Rawnsley, K. (Eds.), *Fractured Reservoirs*, Geological Society, London, Special Publications 270, 55–71. <https://doi.org/10.1144/GSL.SP.2007.270.01.04>.

Rotevatn, A., Tveranger, J., Howell, J., Fossen, H., 2009. **Dynamic investigation of the effect of a relay ramp on simulated fluid flow: geocellular modelling of the Delicate Arch Ramp, Utah.** *Petroleum Geoscience* 15(1), 45-58. <https://doi.org/10.1144/1354-079309-779>.

Sanderson, D.J., Nixon, C.W., 2018. **Topology, connectivity and percolation in fracture networks.** *Journal of Structural Geology* 115, 167–177. <https://doi.org/10.1016/J.JSG.2018.07.011>.

Sanderson, D.J., Nixon, C.W., 2015. **The use of topology in fracture network characterization.** *Journal of Structural Geology* 72, 55–66. <https://doi.org/10.1016/j.jsg.2015.01.005>.

Schueller, S., Braathen, A., Fossen, H., Tveranger, J., 2013. **Spatial distribution of deformation bands in damage zones of extensional faults in porous sandstones: Statistical analysis of field data.** *Journal of Structural Geology* 52, 148–162. <http://dx.doi.org/10.1016/j.jsg.2013.03.013>.

Sénant, J., Popoff, M., 1991. **Early Cretaceous extension in northeast Brazil related to the South Atlantic opening.** *Tectonophysics* 198, 35–46. [https://doi.org/10.1016/0040-1951\(91\)90129-G](https://doi.org/10.1016/0040-1951(91)90129-G).

Shipton, Z. K., Evans, J. P., Thompson, L.B., 2005. **The Geometry and Thickness of Deformation-band Fault Core and its Influence on Sealing Characteristics of Deformation-band Fault Zones.** *American Association of Petroleum Geologists* 85, 181–195. <https://doi.org/10.1306/1033723M853135>.

Silva, J.G.F., Córdoba, V.C., Caldas, L.H.C., 2014. **Proposta de novas unidades litoestratigráficas para o Devoniano da Bacia do Rio do Peixe, Nordeste do Brasil.** *Brazilian Journal of Geology* 44, 561–578. <https://doi.org/10.5327/Z23174889201400040004>.

Silva, J.P., Gomes, I.F., Santos, R F.V.D., Miranda, T.S, Guedes, R.P., Barbosa, J.A., Guimarães, E.X., Beserra, L.B., Guimaraes, L.J.N., 2021. **Topological analysis of**

fracture networks integrated with flow simulation models for equivalent fracture permeability estimation. *Journal of Structural Geology* 147, 104338. <https://doi.org/10.1016/j.jsg.2021.104338>.

Silva, M.E., Nogueira, F.C.C., Pérez, Y.A.R., Vasconcelos, D.L., Stohler, R.C., Sanglard, J.C.D., Balsamo, F., Bezerra, F.H.R., Carvalho, B.R.B.M., Souza, J.A.B., 2022. **Permeability modeling of a basin-bounding fault damage zone in the Rio do Peixe Basin, Brazil.** *Marine and Petroleum Geology*, 135, 105409. <https://doi.org/10.1016/j.marpetgeo.2021.105409>.

Soliva, R., Ballas, G., Fossen, H., Philip, S., 2016. **Tectonic regime controls clustering of deformation bands in porous sandstone.** *Geology* 44, 423–426. <https://doi.org/10.1130/G37585.1>.

Souza, F.M., Gomes, I.F., Nogueira, F.C.C, Vasconcelos, D.L., Canabarro, B., Souza, J.A.B, Guimarães, L.J.N, Beserra, L.B.S., 2022. **2D modeling and simulation of deformation bands' effect on fluid flow: Implications for hydraulic properties in siliciclastic reservoirs.** *Journal of Structural Geology* 158. <https://doi.org/10.1016/j.jsg.2022.104581>.

Stohler, R.C., 2021. **Modelagem numérica 3D do impacto de bandas de deformação no fluxo de escoamento em meio poroso.** Rio de Janeiro, 2021. xix, 208 f. Dissertação – Programa de Pós-graduação em Geologia, Instituto de Geociências, Universidade Federal do Rio de Janeiro.

Stohler, R.C., Nogueira, F.C.C., Mello, C.L., Jorge A. B. Souza, J.A.B., 2022. **3D numerical modelling and simulation of the impact of fault zones on fluid flow in sandstones of the Rio do Peixe Basin, NE Brazil.** *Petroleum Geoscience* 24 (8). <https://doi.org/10.1144/petgeo2022-024>.

Torabi, A., 2007. **Deformation Bands in Porous Sandstone, Their Microstructure and Petrophysical Properties.** PhD thesis. University of Bergen, 153 p. Disponível em: <https://hdl.handle.net/1956/3145>.

Torabi, A., Balsamo, F., Nogueira, F.C.C., Vasconcelos, D.L., Silva, A.C.E., Bezerra, F.H. R., Souza, J.A.B., 2021. **Variation of thickness, internal structure and petrophysical properties in a deformation band fault zone in siliciclastic rocks.**

Marine and Petroleum Geology 133, 105297.
<https://doi.org/10.1016/j.marpetgeo.2021.105297>.

Torabi, A., Berg, S.S., 2011. Scaling of fault attributes: A review. **Marine and Petroleum Geology** 28, 1444–1460.
<https://doi.org/10.1016/j.marpetgeo.2011.04.003>.

Torabi, A., Ellingsen, T.S.S., Johannessen, M.U., Alaei, B., Rotevatn, A., Chiarella, D., 2020. **Fault zone architecture and its scaling laws: where does the damage zone start and stop?** Geological Society of London, Special Publications 496, 99–124.
<https://doi.org/10.1144/SP496-2018-151>.

Torabi, A., Fossen, H., 2009. **Spatial variation of microstructure and petrophysical properties along deformation bands in reservoir sandstones.** American Association of Petroleum Geologists 93, 919–938.
<https://doi.org/10.1306/03270908161>.

Torabi, A., Johannessen, M.U., Ellingsen, T.S.S., 2019. **Fault Core Thickness: Insights from Siliciclastic and Carbonate Rocks.** Geofluids 1–24.
<https://doi.org/10.1155/2019/2918673>.

Tveranger, J., Braathen, A., Skar, T., 2004. **Incorporation of fault zones as volumes in reservoir models.** Bolletino di Geofisica Teoretica et Applicata 45, 316–318.

Vagle, E.B., 2020. **Topology and distribution of deformation bands in normal fault damage zones, Utah.** Master Thesis. University of Bergen, Department of Earth Science. 117.

Vasconcelos, D., Marques, F. O., Nogueira, F. C. C., Perez, Y. A. R., Bezerra, F. H. R., Stohler, R. C., Souza, J. A. B., 2021. **Tectonic inversion assessed by integration of geological and geophysical data: The intracontinental Rio do Peixe Basin, NE Brazil.** Basin Research 2020, 1–24. <https://doi.org/10.1111/bre.12491>.

Wibberley, C.A.J., Pettit, J.P., Rives, T., 2007. **The mechanics of fault distribution and localization in high-porosity sands, Provence, France.** Geological Society of London, Special Publications 289, 19–46. <https://doi.org/10.1144/SP289.3>.

Wilson, P.I.R., Wilson, R.W., Sanderson, D.J., Jarvis, I., McCaffrey, K.J.W., 2021. **Analysis of deformation bands associated with the Trachyte Mesa intrusion, Henry Mountains, Utah: implications for reservoir connectivity and fluid flow around sill intrusions.** *Solid Earth* 12, 95–117. <https://doi.org/10.5194/se-12-95-2>.